

RESEARCH ARTICLE

Neuronal synchrony and the relation between the blood-oxygen-level dependent response and the local field potential

Dora Hermes^{1,2,3*}, Mai Nguyen⁴, Jonathan Winawer^{1*}

1 Department of Psychology, New York University, New York, New York, United States of America, **2** Brain Center Rudolf Magnus, Department of Neurology & Neurosurgery, University Medical Center Utrecht, Utrecht, the Netherlands, **3** Department of Psychology, Stanford University, Stanford, California, United States of America, **4** Department of Psychology, Princeton University, Princeton, New Jersey, United States of America

* dorahermes@gmail.com (DH); jonathan.winawer@nyu.edu (JW)



OPEN ACCESS

Citation: Hermes D, Nguyen M, Winawer J (2017) Neuronal synchrony and the relation between the blood-oxygen-level dependent response and the local field potential. *PLoS Biol* 15(7): e2001461. <https://doi.org/10.1371/journal.pbio.2001461>

Academic Editor: Adam Kohn, Albert Einstein College of Medicine, United States of America

Received: December 9, 2016

Accepted: June 22, 2017

Published: July 24, 2017

Copyright: © 2017 Hermes et al. This is an open access article distributed under the terms of the [Creative Commons Attribution License](https://creativecommons.org/licenses/by/4.0/), which permits unrestricted use, distribution, and reproduction in any medium, provided the original author and source are credited.

Data Availability Statement: ECoG and fMRI data are available for download on <https://osf.io/v22bm/>. Code to download these data, run the simulations, and reproduce the figures can be found on https://github.com/dorahermes/Paper_Hermes_2017_PLOSbiology. The ECoG data, which was previously published and re-analyzed for this paper, was provided as part of the Stanford Human Intracranial Cognitive Epilepsy Program (SHICEP), headed by Josef Parvizi.

Funding: NIH <https://www.nei.nih.gov/> (grant number T32-EY20485). Received by DH. The

Abstract

The most widespread measures of human brain activity are the blood-oxygen-level dependent (BOLD) signal and surface field potential. Prior studies report a variety of relationships between these signals. To develop an understanding of how to interpret these signals and the relationship between them, we developed a model of (a) neuronal population responses and (b) transformations from neuronal responses into the functional magnetic resonance imaging (fMRI) BOLD signal and electrocorticographic (ECoG) field potential. Rather than seeking a transformation between the two measures directly, this approach interprets each measure with respect to the underlying neuronal population responses. This model accounts for the relationship between BOLD and ECoG data from human visual cortex in V1, V2, and V3, with the model predictions and data matching in three ways: across stimuli, the BOLD amplitude and ECoG broadband power were positively correlated, the BOLD amplitude and alpha power (8–13 Hz) were negatively correlated, and the BOLD amplitude and narrowband gamma power (30–80 Hz) were uncorrelated. The two measures provide complementary information about human brain activity, and we infer that features of the field potential that are uncorrelated with BOLD arise largely from changes in synchrony, rather than level, of neuronal activity.

Author summary

There are several methods for measuring activity in the living human brain. Here, we studied functional magnetic resonance imaging (fMRI), which depends on the vascular response to neuronal activity, and surface field potentials, which measure electrical activity from many neurons. These two widely used measurements of human brain activity often provide different and potentially conflicting results. We propose a quantitative model for how these two measurements integrate activity from neuronal populations. The fMRI signal is highly sensitive to the average level of local neuronal activity but not the

funder had no role in study design, data collection and analysis, decision to publish, or preparation of the manuscript. NIH <https://www.nei.nih.gov/> (grant number R00-EY022116). Received by JW. The funder had no role in study design, data collection and analysis, decision to publish, or preparation of the manuscript. NIH www.nimh.nih.gov (grant number R01MH111417-01). Received by JW. The funder had no role in study design, data collection and analysis, decision to publish, or preparation of the manuscript. Netherlands Organization for Scientific Research www.nwo.nl (grant number 016.VENI.178.048). Received by DH. The funder had no role in study design, data collection and analysis, decision to publish, or preparation of the manuscript.

Competing interests: The authors have declared that no competing interests exist.

Abbreviations: BOLD, blood-oxygen-level dependent; ECoG, electrocorticographic; EEG, electro-encephalography; fMRI, functional magnetic resonance imaging; LFP, local field potential; L/N, linear/nonlinear; MEG, magneto-encephalography; MUA, multiunit spiking activity; pRF, population Receptive Field.

degree of synchrony between neurons. In contrast, the field potential is most sensitive to synchronous neuronal signals. Our model accounts for several observations seen in fMRI and field potential data: some very large features of field potential recordings, such as gamma oscillations, can occur with little to no associated fMRI signal. The model predicts this because the gamma oscillations result more from increased neuronal synchrony than increased neuronal activity. Other field potential signals, such as broadband changes, which are likely driven by the level of neuronal activity rather than a change in synchrony, are highly correlated with fMRI. The two measures thus provide complementary information about human brain activity.

Introduction

Most measurements of activity in the living human brain arise from the responses of large populations of neurons, spanning the millimeter scale of functional magnetic resonance imaging (fMRI) and electrocorticography (ECoG) to the centimeter scale of electro- and magneto-encephalography (EEG and MEG). Integrating results across methods is challenging because the signals measured by these instruments differ in spatial and temporal sensitivity, as well as in the manner by which they combine the underlying neuronal population activity [1–3]. Differences in scale can be partially bridged by bringing the measurements into register. For example, EEG and MEG sensor data can be projected to cortical sources subject to constraints from simultaneously recorded fMRI data [4] or from independent fMRI localizers [5], and ECoG electrodes can be aligned to a high-resolution anatomical MRI image [6] and compared to the local fMRI signal.

Yet, even when electrophysiological and fMRI data are spatially registered, striking differences in the sensitivity to stimulus and task are often observed, indicating differences in how neuronal responses contribute to the measured physiological signals. For example, the fMRI blood-oxygen-level dependent (BOLD) signal and EEG evoked potentials differ in which brain areas are most sensitive to visual motion (area MT+ with fMRI [7] versus V1 and V3A with EEG [8]). Within the same visual area, fMRI and source-localized EEG evoked potentials can show different effects of task in similar experimental paradigms, such as the effect of spatial attention on the contrast response function (additive in fMRI [9], multiplicative in EEG [10]). Even when the spatial scale of the two signals is approximately matched at acquisition, such as ECoG electrodes and fMRI voxels (both at approximately 2 mm), systematically different patterns of responses can be obtained, such as compressive spatial summation in fMRI versus nearly linear summation in ECoG steady-state potentials (but not ECoG broadband signals) [11]. Such fundamental functional differences cannot be explained by numerical measurement-to-measurement transformations. Rather, these differences must reflect the fact that the measurements are based on different aspects of the neural population response. To explain the differences in measurement modalities requires a computational framework that derives each of these signals from the neuronal responses.

One approach toward developing such a framework has been to measure the BOLD signal and electrophysiological signals simultaneously, or separately but using the same stimulus and task conditions, and to ask how features of the electrophysiological response compare to the BOLD signal. This approach has revealed important patterns, yet after several decades of careful study, some apparent discrepancies remain. A number of studies comparing band-limited power in field potential recordings to the BOLD signal have shown that increases in power between 30 Hz and 100 Hz (gamma band) are more highly correlated with BOLD amplitude

than power changes in other bands [12–17]. Yet, power changes in this band do not fully account for the BOLD signal: very large power changes can occur in the gamma band without a measurable BOLD signal change [18, 19], and power changes in lower frequency bands can be correlated with the BOLD signal independently of power changes in the gamma band [20–23]. It therefore cannot be the case that field potential power in the gamma band is a general predictor of BOLD, even if the two measures are often correlated. Another source of disagreement is that within the gamma band, some reports claim that BOLD is best predicted by synchronous (narrowband) signals [13], and others claim that BOLD is best predicted by asynchronous (broadband) neural signals [11]. Moreover, in some cases, it has been reported that no feature of the local field potential (LFP) predicts the intrinsic optical imaging signal (closely related to BOLD) as accurately as multiunit spiking activity [24]. Consistent with this claim, a comparison of both motion and contrast response functions measured with single units and with BOLD suggested a tight coupling between BOLD and single-unit responses [25–27]. To our knowledge, there is currently no single model linking the electrophysiological and BOLD signals that accounts for the wide range of empirical results.

The numerous studies correlating features of electrophysiological signals with BOLD provide constraints in interpreting the relationship between the two types of signals, yet the approach has not led to a general, computational solution. We argue that one reason that correlation studies have not led to computational solutions is that any particular feature of the field potential could be caused by many possible neuronal population responses. For example, a flat field potential (minimal signal) could arise because there is little activity in the local neuronal population or it could arise from a pair of neuronal subpopulations responding vigorously but in counterphase, resulting in cancellation in the field potential. The same field potential in the two situations would be accompanied by different levels of metabolic demand and presumably different levels of BOLD signal. Similarly, any particular BOLD measurement could be due to many different patterns of neural activity. For example, stimulation of a neuronal population that inhibits local spiking can cause an elevation in the BOLD signal [28], as can stimulation of an excitatory population that increases the local spike rate [29]. In short, there can be no single transfer function that predicts the BOLD signal from the field potential because the field potential does not **cause** the BOLD signal; rather, the neuronal activity gives rise to both the field potential and the BOLD signal.

We propose that many of the different claims pertaining to the relationship between BOLD amplitude and features of the field potential can be accounted for by a modeling framework in which BOLD and field potential measurements are predicted from simulated neuronal population activity, rather than by predicting the BOLD signal directly from the field potential. In this paper, we model fMRI and ECoG responses in two stages, one stage in which we simulate activity in a population of neurons, and a second stage in which we model the transformation from the population activity to the instrument measures. By design, the model employs a minimal set of principles governing how the instruments pool neuronal activity, rather than a biophysically detailed description of neuronal and hemodynamic events. This approach enables us to ask whether this minimal set of principles is sufficient to guide simulations of neuronal population activity, such that the parameters of the simulations are fit to ECoG measurements from human visual cortex, and the output of the simulations predicts fMRI BOLD responses in the same regions for the same stimuli.

Results

We first present an analytic framework to capture basic principles of how the BOLD signal and the field potential pool neuronal signals across a population (2.1). Using this framework,

we derive equations for the relationship between each instrument measure (BOLD and LFP) and the underlying neuronal activity, as well as the relationship between the instrument measures. This section shows that synchrony is expected to have a large effect on the LFP signal but not on the BOLD signal. The analytic framework provides a way to derive the instrument measures from neuronal population activity, but it does not specify the neuronal population activity itself. In the next section (2.2), we develop a method for simulating neuronal population time series from a small number of parameterized inputs, and we show how the simulated neuronal activity can be converted to (simulated) LFP and BOLD by applying the equations derived in 2.1. Next, we fit parameters for simulating population neuronal activity using ECoG data from human V1, V2, and V3 and compare the BOLD responses derived from these simulations to measured BOLD responses from V1, V2, and V3 (2.3). Finally, we quantify the relationship between simulated BOLD and LFP, and between measured BOLD and ECoG, and show that the same patterns hold for simulation and data (2.4).

2.1 Relationship between LFP and BOLD: Analytic framework

The fMRI BOLD signal and the LFP measure neuronal population activity in a fundamentally different manner. The goal of this analytic framework is to capture these differences in simple mathematical expressions and from these expressions, derive the relationship between the two instrument measurements. We purposely omit a large number of biophysical details, such as cell types, neuronal compartments, the dynamics of blood flow, and so forth, both for tractability and in order to emphasize the basic principles of how different measures integrate neuronal activity. In the sections that follow, we then show that, when coupled to simulated neural responses, the model can account for many important patterns observed in fMRI and ECoG data from human visual cortex.

For this analytic framework, we consider how a population of n neurons responds to a stimulus or task during a brief epoch (time 0 to T), assumed to be on the order of a second. Each neuron will produce a time-varying dendritic current, denoted as $I_i(t)$ for the i th neuron, resulting from the trans-membrane potential. We would like to know how these currents, $I(t)$, relate to the fMRI BOLD signal and to the LFP signal measured by an ECoG electrode.

We assume that the LFP arises primarily from dendritic membrane currents [2]. We ignore output spikes. (Although spikes can influence the LFP [30], it is generally thought that the influence is smaller than synaptic and dendritic currents [2], and including spikes would not change the logic of our arguments.) For the i th neuron, the contribution to the LFP is then $\alpha_i \times I_i(t)$. The constant α_i depends on the distance and orientation of the neuron with respect to the electrode, as well as the electrode's impedance. For simplicity, we assume that each neuron is equidistant from the electrode and has the same orientation, like pyramidal neurons perpendicular to the cortical surface, and therefore its contribution to the electrode measurement is scaled by the same constant, α . These neurons act together like a single, equivalent circuit, and hence the LFP time series will sum the contribution from each neuron,

$$LFP(t) = \alpha \cdot \sum_i^n I_i(t) \tag{Eq 1}$$

Field potential recordings are often summarized as the power (or band-limited power) in the time series [31]. Here we summarize the LFP response within a short time window as the power in the signal summed over the time window T :

$$LFP \text{ power} = \alpha \cdot \int_0^T ([\sum_i^n I_i(t)]^2) dt \tag{Eq 2}$$

power of sum

Importantly, Eq 2 is a linear/nonlinear (L/N) computation, since the LFP power is computed by first summing the signals (L), and then computing the power (N).

The BOLD signal pools neural activity in a fundamentally different manner because it depends on metabolic demand [e.g., for reviews, see 1, 32]. (Recent work on the neurobiology of neurovascular coupling indicates that much of the BOLD signal is not caused directly by changes in the level of metabolic products such as glucose, but rather by signaling molecules that tend to correlate with metabolic demand [33]). For simplicity, we discuss the BOLD signal throughout in terms of metabolic demand and return to this issue explicitly in the Discussion, (3.6 The role of a simple model in understanding the relation between BOLD and LFP). The metabolic demand of each neuron will increase if the cell depolarizes (excitation) or hyperpolarizes (inhibition) [28, 34, 35]. Hence, the metabolic demand of a neuron is a **nonlinear** function of its membrane potential: either a positive or negative change in voltage relative to resting potential causes a current, thereby resulting in a positive metabolic demand. There are many possible nonlinear functions one could assume to summarize the metabolic demand from the dendritic time series, such as the rectified signal (absolute value) or the power (squared signal). For tractability, we assume the metabolic demand of the i th neuron is proportional to the power in the time-varying trans-membrane current integrated over time: $\beta_i \times (POWER(I_i(t)))$ or $\beta_i \times \int_0^T (I_i(t)^2) dt$, with β_i a scaling constant for the i th neuron. (Similar results were obtained if we used the absolute value rather than the power). For the entire population of n neurons, we then assume the BOLD signal will sum the metabolic demand of each neuron. For simplicity, we use the same scaling constant for each neuron:

$$BOLD = \beta \cdot \sum_i^n (\int_0^T (I_i(t)^2) dt) \tag{Eq 3}$$

sum of power

Importantly, Eq 3 is an N/L computation, since the power is computed first (N) and then the signals are summed (L), opposite to the order of operations for the LFP in Eq 3 (Fig 1) (personal communication from David J Heeger). In other words, we approximate the BOLD signal as the sum of the power, and LFP as the power of the sum, of the separate neuronal time series. The difference in the order of operations can have a profound effect on the predicted signals, as in the simple example with two neurons depicted in Fig 1C and 1D. The BOLD signal pooled over the two neurons is the same whether the time series from the two neurons are in phase or out of phase, whereas the LFP power is large when the time series are in phase and small when they are out of phase.

These approximations allow us to make predictions about the relation between LFP and BOLD. By theorem, we know that the power of the sum of several time series is exactly equal to the sum of the power of each time series plus the sum of the cross-power between the different time series (Eq 4):

$$\int_0^T ([\sum_i^n X_i(t)]^2) dt = \sum_i^n (\int_0^T (X_i(t)^2) dt) + \sum_{i \neq j}^n (\int_0^T (X_i(t) \cdot X_j(t)) dt) \tag{Eq 4}$$

Power of sum Sum of power Sum of cross – power

Applying this theorem to Eqs 2 and 3 shows the relationship between our models of BOLD and LFP power:

$$LFP\ power = \alpha / \beta \cdot BOLD + \alpha \cdot \sum_{i \neq j}^n (\int_0^T (I_i(t) \cdot I_j(t)) dt) \tag{Eq 5}$$

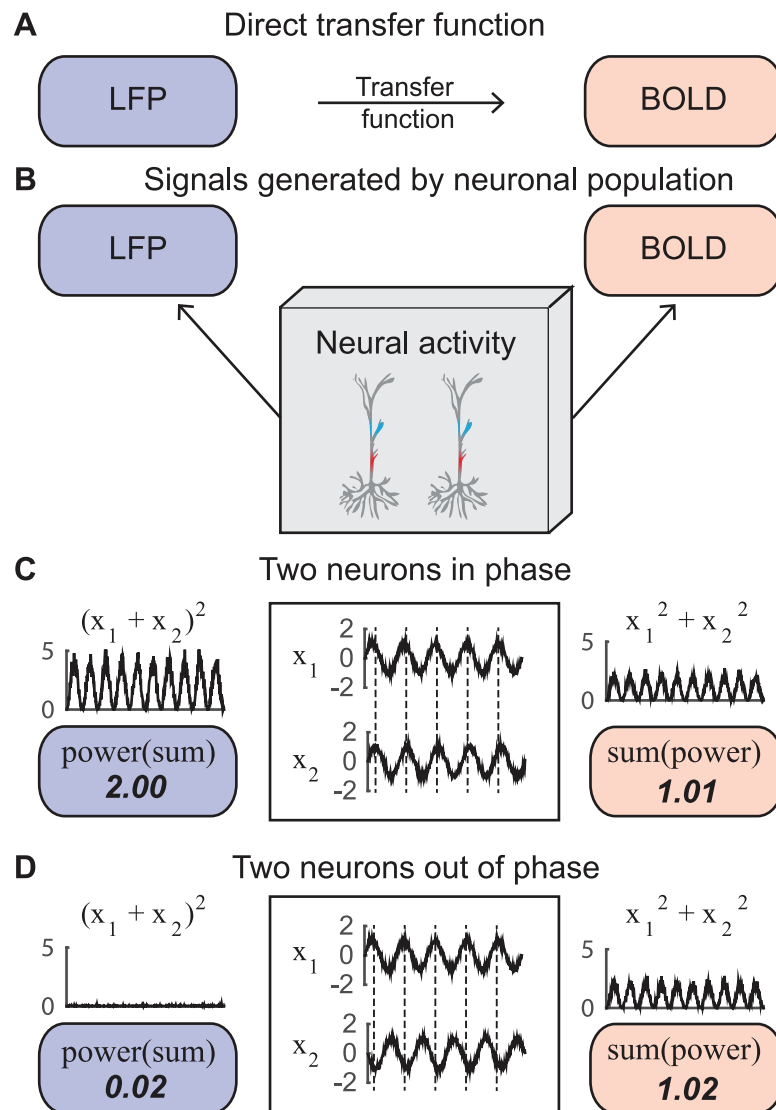


Fig 1. Pooling with different orders of operations can have a large effect on measured brain signals. (A) The approach to directly correlate local field potential (LFP) and blood-oxygen-level dependent (BOLD) data. (B) The current approach to relate the LFP and BOLD from the same neuronal population activity. (C) In this illustration, the currents of two neurons (x_1 and x_2) has the shape of a sinusoid with noise, and the sinusoid is in phase between the two neurons. In the simulated electrode measurement, the signals are summed and the power is calculated ($\text{POWER}[\text{SUM}] = 2.00$). In the simulated measurement of metabolic demand, the power of each of these neurons is first calculated and then summed across the neurons ($\text{SUM}[\text{POWER}] = 1.01$). Here, the LFP and BOLD are both large. (D) In this illustration, the membrane currents of two neurons (x_1 and x_2) are the same as in panel (C) except that the two time series are in counterphase. Here, unlike (C), the LFP is nearly 0 and the BOLD signal is large (code to reproduce this figure can be found on https://github.com/dorahermes/Paper_Hermes_2017_PLOSbiology function ns_script01_Fig1.m).

<https://doi.org/10.1371/journal.pbio.2001461.g001>

We can now see that the LFP power depends on two quantities, one of which is related to the BOLD signal, and one of which is unrelated to the BOLD signal (Eq 5). The first quantity summarizes the total level of neural activity (summed across neurons), and the second quantity summarizes the relationship between neural time series (the cross-power, similar to

covariance). If and when the second term tends to be large compared to the first, then the LFP power will not be closely related to the BOLD signal.

One cannot deduce from first principles whether the first term in Eq 4 (summed power) or the second term (summed cross-power) will dominate. However, the number of elements contributing to the two terms is quite different: For n neurons, the first term has n numbers (the power in each neuron's time series), whereas the second term has nearly n^2 numbers (all the pairwise cross-powers). Hence, if there is any appreciable covariance, then the LFP power will be dominated by the second term, and the correlation with BOLD will be weak (except in cases where the cross-power and power are highly correlated).

To see how these equations translate to quantitative measures of BOLD and LFP, we consider a small neuronal population whose time series conform to a multivariate Gaussian distribution. We assume that each neuron's time series has the same mean, m ; the same variance, σ^2 ; and all of the pairwise correlations have the same value, ρ :

$$\begin{aligned}
 X &\sim \mathcal{N}(\mu, \Sigma) \\
 \mu &= \begin{pmatrix} m \\ \vdots \\ m \end{pmatrix} \\
 \Sigma &= \begin{bmatrix} \sigma^2 & \cdots & \sigma^2 \rho \\ \vdots & \ddots & \vdots \\ \sigma^2 \rho & \cdots & \sigma^2 \end{bmatrix}
 \end{aligned} \tag{Eq 6}$$

X is the population time series, μ is the mean of each time series, and Σ is the covariance matrix. We can now rewrite the simulated BOLD signal (the sum of the power) and the LFP (power of the sum) in terms of the parameters of the multivariate Gaussian (and arbitrary scaling factors α, β),

$$\begin{aligned}
 BOLD &= \beta \cdot [n \cdot (m^2 + \sigma^2)] \\
 LFP \text{ power} &= \alpha \cdot [n \cdot (m^2 + \sigma^2) + (n^2 - n)(m^2 + \sigma^2 \rho)]
 \end{aligned} \tag{Eq 7}$$

where n is the number of neurons. This enables us to visualize how the BOLD signal and the LFP power depend on just three values: the variance, correlation, and mean in the neural time series, rather than on all the individual time series (Fig 2). For these neuronal time series, the LFP, modeled as the power of the sum of neuronal time series (panel A), is dominated by the neuronal cross-power (panel C). The BOLD signal, modeled as the sum of the power in the neuronal time series (panel B), makes little contribution to the LFP, except when the correlation between neurons is low (ρ is close to 0); in this case, there is no cross-power, and BOLD and LFP power are correlated.

2.2 Simulating the LFP and BOLD responses

In section 2.1, we proposed formulae to derive instrument measures from neuronal population activity. Here, we ask how we might simulate neuronal activity with a small number of parameters. A low-dimensional characterization of the population activity is useful since we normally do not have access to the time series of an entire population of neurons. Moreover, a low-dimensional representation can lead to better understanding and generalization even when high-dimensional data are available [36, 37]. After simulating the population activity, we then

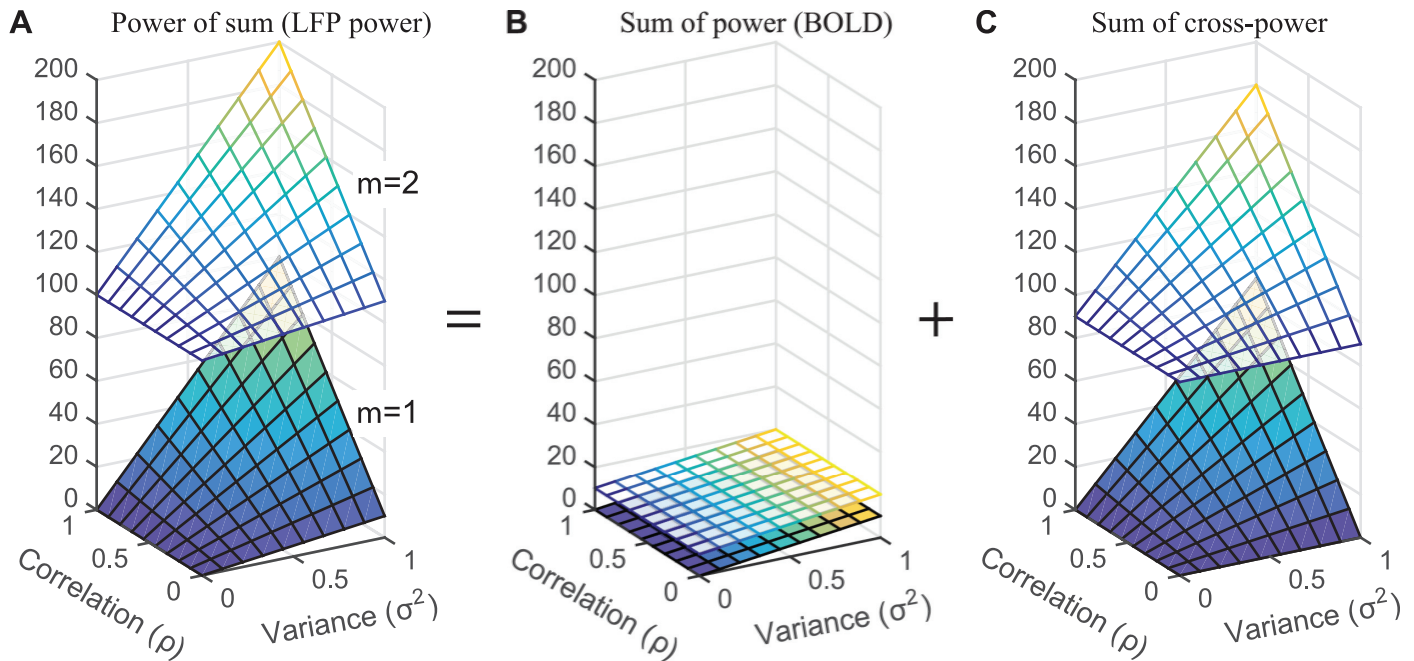


Fig 2. The influence of time series parameters on the power of the sum, the sum of the power, and the cross-power. (A) LFP power, computed as the power of the sum of 5 time series from a multivariate Gaussian distribution (Eq 6). The LFP power is shown as a function of the correlation (ρ), variance (σ), and mean (μ) of the time series (Eq 7). (B) The same as A, except plotting the sum of the power rather than the power of the sum, in order to model the BOLD signal. (C) The same as B but for cross-power. The power of the sum—Panel A—is the sum of the terms in Panels B & C. (Code to reproduce this figure can be found on https://github.com/dorahermes/Paper_Hermes_2017_PLOSbiology function ns_script02_Fig2.m).

<https://doi.org/10.1371/journal.pbio.2001461.g002>

use the analytic framework from section 2.1 to compute the BOLD and LFP signals. The parameters for the simulations were fit to ECoG recordings from human V1, V2, and V3 [38]. Because there were recordings from multiple electrodes and multiple stimuli, we ran multiple simulations fit to the different ECoG responses. We then used these simulations to predict the BOLD signal and compared these predictions to the measured BOLD signal for the same stimuli and same cortical locations (but in different observers). The steps for simulating the neuronal population data and the derived LFP and BOLD, and for comparing the simulations to empirical data, are summarized in Table 1.

In the ECoG experiments, there were four grating stimuli of different spatial frequencies, three noise patterns with different power spectra, and one blank stimulus (mean luminance). For each of the 8 stimuli and each of 22 electrodes in V1, V2 and V3, we decomposed the measured ECoG responses into three spectral components: broadband, narrowband gamma, and alpha (Fig 3). An important feature of this dataset is that the three components of the ECoG responses showed different patterns across stimuli [38]: stimuli comprised of noise patterns caused large broadband increases but little to no measureable narrowband gamma response, whereas grating stimuli elicited both broadband increases and narrowband gamma increases. Gratings and noise stimuli both resulted in decreases in alpha power compared to baseline (also see S1 Fig). Had all three responses been tightly correlated with each other, it would not be possible to infer how each relates separately to the BOLD signal.

2.2.1 Simulations of BOLD and LFP responses from neuronal population activity.

Cortical neurons receive a large number of inputs from diverse cell types. For our low-dimensional parameterization of the population activity, we assumed that each neuron received a mixture of three types of inputs (Fig 4A). These three inputs, following summation and leaky

Table 1. A summary of analysis steps for simulations (MODEL) and comparison to data (DATA).

Analysis	Figure
1. DATA: LFP spectral components. ECoG responses in visual cortex are separated into the sum of three spectral components: broadband, narrowband gamma, and narrowband alpha, yielding three numbers per electrode per stimulus.	Fig 3
2. MODEL: Inputs. We propose three classes of signals, “C1,” “C2,” and “C3,” as inputs to simulated individual neurons. These are like basis functions, as responses to each stimulus will be modeled with different mixtures of C1, C2, and C3 inputs (Step 5).	Fig 4A
3. MODEL: Neural activity. Neural responses to C1, C2, and C3 inputs are simulated with a population of neurons with leaky integration.	Fig 4B and 4C
4. MODEL: LFP spectral components. The simulated neuronal activity in the population is converted to simulated LFP. The LFP spectra arising from C1, C2, and C3 inputs approximate the three LFP components observed in ECoG data (step 1 above).	Fig 5
5. MODEL: Parameters. The model parameters are the levels of C1, C2, and C3 inputs. These are fit to the observed ECoG data for each stimulus and each electrode. This results in three numbers per electrode per stimulus.	Fig 6
6. MODEL: Predictions. These model neural inputs are converted to simulated neuronal activity and then to simulated BOLD responses.	Fig 4D; Fig 7A and 7B (x-axis)
7. MODEL: Accuracy and DATA. These simulated BOLD responses are compared with <i>real, measured BOLD responses</i> .	Fig 7A and 7B (y-axis); Fig 7C
8. MODEL: LFP–BOLD relationship. The simulated BOLD responses are also fit to simulated LFP responses with a regression model.	Fig 8C and 8D; Fig 9C and 9D
9. DATA: LFP–BOLD relationship. <i>Real measured BOLD responses are also fit to measured ECoG LFP components using a regression model.</i>	Fig 8A and 8B; Fig 9A and 9B

BOLD, blood-oxygen-level dependent; ECoG, electrocorticographic; LFP, local field potential

<https://doi.org/10.1371/journal.pbio.2001461.t001>

integration, produce the three spectral components observed in the ECoG data. Input 1 approximated Poisson-like spike arrivals (C^1 , “Broadband”) and had a mean above 0 (excitatory). Input 2 was a high-frequency oscillation, peaked between 40 Hz and 60 Hz, coordinated between neurons (C^2 , “Gamma”), with a mean of 0. Input 3 was a low-frequency signal peaked between 8 Hz and 12 Hz that was inhibitory: i.e., the mean was below 0 (C^3 , “Alpha”).

For each simulated neuron i , the total input C on each trial is the sum of these three signals (Fig 4B):

$$C_i(t) = C_i^1(t) + C_i^2(t) + C_i^3(t) \quad (\text{Eq 8})$$

We then passed the summed input in each neuron through a leaky integrator to produce the time-varying dendritic current for that neuron (I_i , Fig 4C):

$$\tau \cdot \frac{dI_i}{dt} = -I_i(t) + C_i(t) \quad (\text{Eq 9})$$

The membrane time constant τ reflects the time dependence of the trans-membrane current [39, 40]. In total, we modeled a population of 200 neurons, each of which produced a 1-second time series on each trial. From the neuronal population simulations, we computed the LFP and BOLD signals according to the equations above (section 2.1 “Relationship between LFP and BOLD: Analytic framework”). In brief, the LFP was computed by summing the trans-membrane current across neurons (Eq 1, Fig 4C), and the BOLD signal was computed by summing the power across neurons (Eq 3, Fig 4D). The LFP was used as training

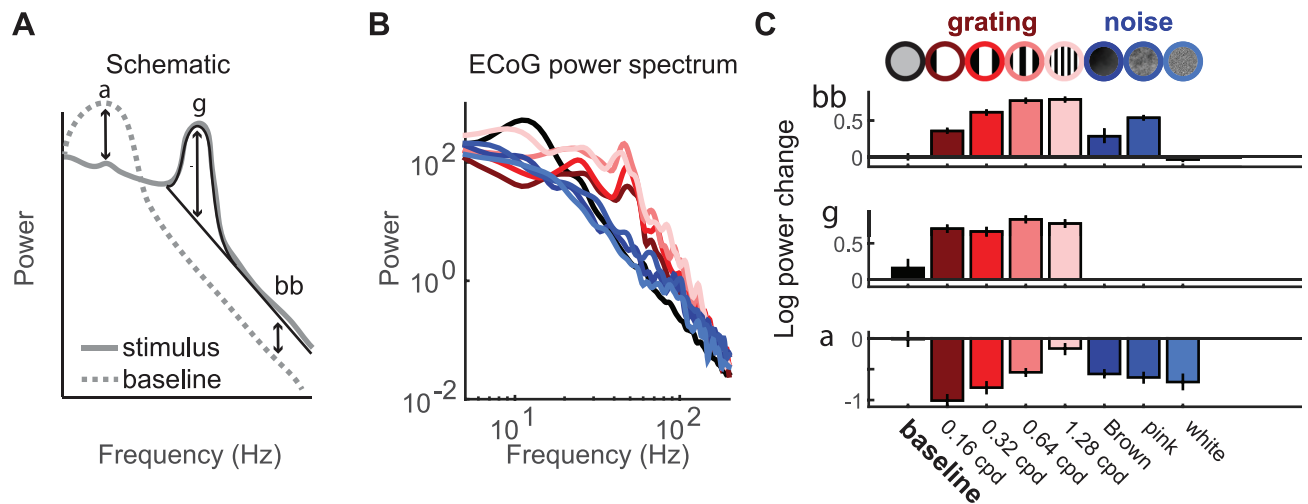


Fig 3. Decomposing electrocorticographic (ECoG) data into three summary components. (A) A schematic to show the summary metrics derived from ECoG spectra: broadband power elevation (bb), narrowband gamma (γ), and alpha (α). Broadband was calculated by the increase in a $1/f^n$ signal, gamma was calculated by fitting a Gaussian on top of the $1/f^n$ line, and alpha was calculated as the difference from baseline in the alpha-frequency range. (B) Power spectrum for one example electrode during a blank stimulus (black), gratings (red), and noise patterns (blue). (C) From the power spectrum, changes in broadband, gamma, and alpha were calculated. These values were bootstrapped 100 times across trials. Error bars represent 68% confidence intervals. (code to download data and reproduce this figure can be found on https://github.com/dorahermes/Paper_Hermes_2017_PLOSbiology function ns_script03_Fig3.m).

<https://doi.org/10.1371/journal.pbio.2001461.g003>

data (to fit the parameters of the inputs), and the BOLD signal was used as test data (to test the accuracy of the model).

2.2.2 Simulation inputs produce three effects in the LFP power spectrum. Below, we explain how the time series was generated for each of the three types of inputs and what kind of effect a change in each input has on the power spectrum.

Broadband input (C^1). Input C^1 was Gaussian white noise with a small positive bias. The Gaussian white noise approximates Poisson-distributed spike arrivals, each of which produces a small positive or negative conductance change, corresponding to excitatory or inhibitory postsynaptic potentials. The small positive bias reflects the assumption of more excitatory than inhibitory synaptic currents, causing a net depolarization. Gaussian white noise was used

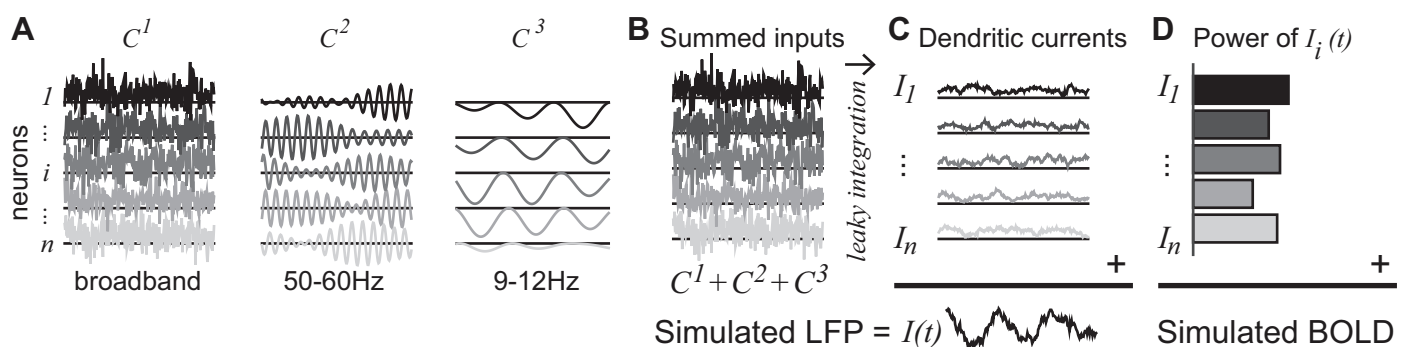


Fig 4. Simulated local field potential (LFP) and blood-oxygen-level dependent (BOLD). (A) Three different inputs to each neuron were simulated: a broadband, random input with a small positive offset (C^1), an oscillatory input with a time scale of 40 Hz to 60 Hz (C^2), and a negative input with a time scale of 10 Hz (C^3). (B) The 3 inputs (C^1 , C^2 , C^3) were summed in each neuron to produce the total input to the neuron. (C) The total input was passed through a leaky integrator to produce the dendritic dipole current (I_i). The LFP was simulated by summing the dendritic currents. (D) The BOLD signal was simulated by taking the power of the dendritic current for each neuron and then summing across neurons. (Code to simulate data reproduce this figure can be found on https://github.com/dorahermes/Paper_Hermes_2017_PLOSbiology function ns_script07D_Fig4.m).

<https://doi.org/10.1371/journal.pbio.2001461.g004>

rather than Poisson-distributed synaptic inputs for computational efficiency, but the pattern of results is similar for Poisson or Gaussian distributions. For the purposes of simulations, we defined a high value of C^1 as high variance in the Gaussian distribution and low values of C^1 as low variance. This mimics the effect of high versus low rates of spike arrivals. The time series for the 200 neurons was generated from a distribution with 0 correlation for all pairs of neurons. Because the variance differed across simulations, and the correlations were always 0, the possible C^1 values span a vertical slice of the plots in Fig 2 (ρ -axis = 0). This white noise input, after passing through leaky integration, results in an output whose power spectral density declines with temporal frequency. When this input increases (higher variance), the result is a broadband elevation in power [40] (Fig 5A). Such broadband power elevations can be observed in the LFP [41] as well as intracellular membrane potentials of single neurons in awake macaque [42].

Gamma input (C^2). Input C^2 consisted of band pass noise (40 Hz to 60 Hz), with fixed amplitude on all trials and with coherence across neurons that varied between trials. This input approximates the signals giving rise to narrowband gamma oscillations. Across different conditions, we varied the correlation between neurons of C^2 rather than the amplitude for individual neurons, which was fixed. This corresponds to a slice in the plots in Fig 2 such that the variance axis is fixed at a nonzero value. The motivation for this comes from empirical observations that large gamma oscillations in the LFP tend to reflect increased coherence between neurons [43, 44]. This is opposite to the broadband input (C^1), for which we varied the amplitude (variance) in individual neurons across trials, rather than the synchrony between neurons. Narrowband gamma oscillations with a peak between 30 Hz and 80 Hz can be observed in the LFP [45, 46] as well as in the membrane potential of individual pyramidal neurons [47]. When we increase the correlation of C^2 in our simulations, the result is an increase in the amplitude of the LFP in the gamma band (Fig 5B), much like narrowband gamma signals observed in microelectrode recordings [48] and human ECoG [38].

Alpha input (C^3). The alpha input consisted of inhibitory oscillations at approximately 10 Hz, with fixed correlation between neurons and varying amplitude across conditions. This corresponds to a slice in the plots in Fig 2 in which the ρ -axis is fixed at a nonzero value. The oscillations were inhibitory, i.e., the mean was below 0 (compare C^3 versus C^1 and C^2 in Fig 4). Because C^3 was inhibitory, it resulted in less depolarization (or hyperpolarization in extreme cases), opposite the effect of C^1 , which resulted in depolarization. This input approximates the signals giving rise to alpha oscillations (Fig 5C). Pyramidal neurons in visual cortex have been hypothesized to receive periodic inhibition, with pulses arriving at approximately 10 Hz [49, 50]. Individual neurons in visual cortex can indeed show subthreshold membrane oscillations at frequencies around 10 Hz [51].

2.3 Fitting the simulation parameters to ECoG responses and predicting BOLD data

The simulations were structured to approximate the experimental design and the results of our ECoG experiments. To match the design of our ECoG experiments, a simulated experiment consisted of 240 trials, each of which were 1 second long (30 repeats of 8 conditions). The LFP time series were transformed to power spectra, which were averaged across the 30 repeated trials of the same condition. The simulation parameters—i.e., the level of the three inputs, C^1 , C^2 , and C^3 —were fit to the measured ECoG summary metrics (broadband, gamma, and alpha) for each of the 8 conditions for a particular electrode (Fig 6). To verify the validity of this procedure, we asked whether the simulations using the fitted parameters produce simulated spectra, which, when analyzed like the ECoG spectra, reproduce the original values of broadband,

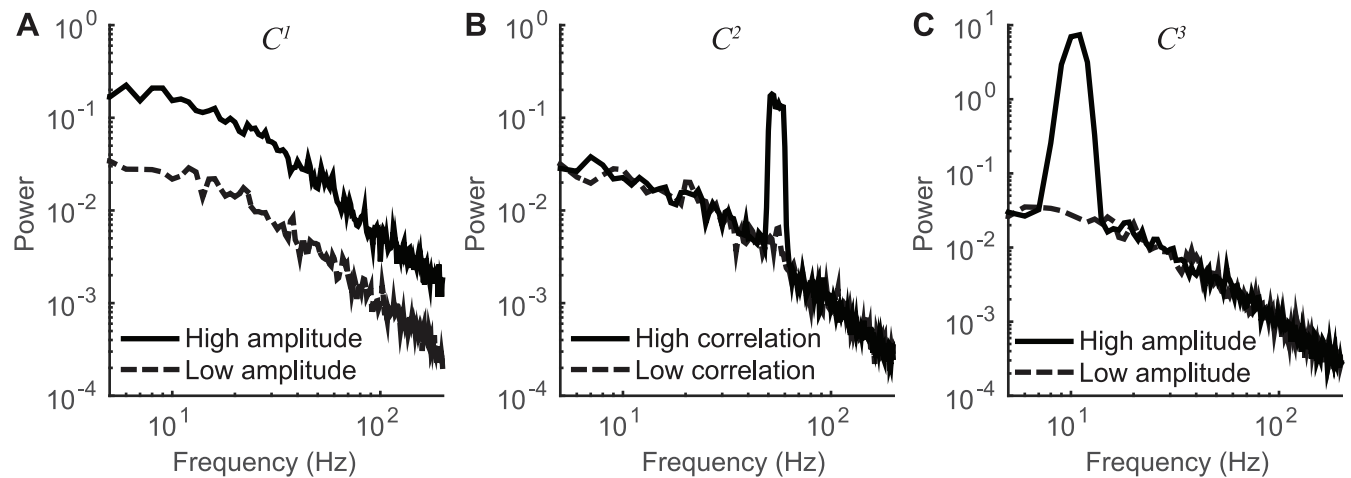


Fig 5. The effect of varying simulated neural inputs on output spectra. The effect of manipulating one of the three neural inputs used in the simulations produced different effects in the spectral power of the local field potential (LFP) of 200 neurons. (A) For C^1 (broadband), a high amplitude results in a broadband power elevation, with no narrow peaks in the spectrum. (B) For C^2 (gamma), a high correlation results in a narrowband gamma power elevation, with no broadband elevation or change in alpha power. (C) For C^3 (alpha), a high amplitude input results in a narrowband power elevation in the alpha band, with no change in broadband power or narrowband gamma power. For each spectrum in each plot, 10 simulated trials were run. The plotted spectra are averaged across the 10 trials and are computed from $I(t)$, the time series after leaky integration of the inputs. (Code to reproduce this figure can be found on https://github.com/dorahermes/Paper_Hermes_2017_PLOSbiology function ns_script05_Fig5.m).

<https://doi.org/10.1371/journal.pbio.2001461.g005>

gamma, and alpha. In other words, do we close the loop from measured spectral components (broadband, gamma, and alpha) to inferred input parameters (C^1 , C^2 , C^3) to simulated population activity, to simulated spectral components (broadband, gamma and alpha)? The original

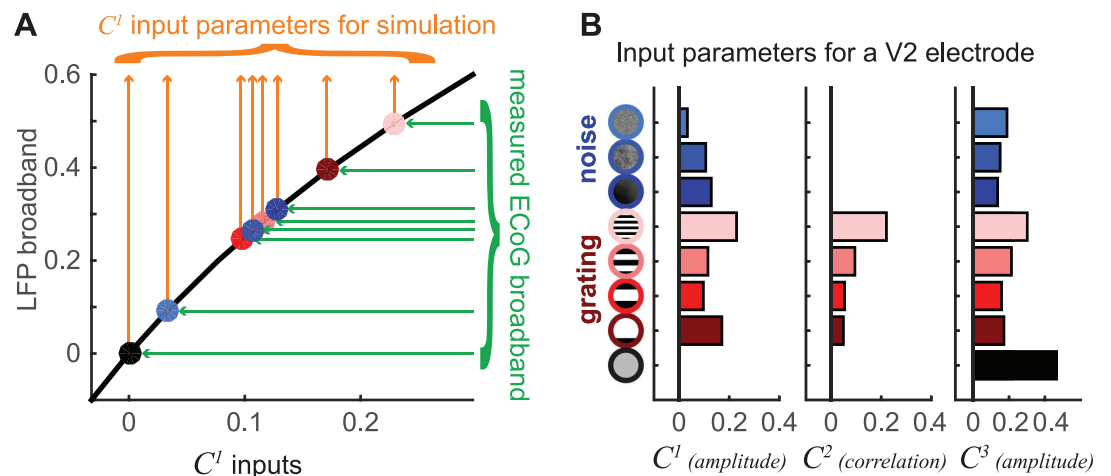


Fig 6. Parameter fits for simulations. (A) A function was fit between the C^1 input and the simulated broadband output (black line). Inverting this function allows us to take the measured electrocorticographic (ECoG) broadband values (green arrows to dots colored by stimulus condition) and convert these into estimates of the C^1 input levels (orange arrows). Because the simulations contain noise, the predicted broadband need not match the measured broadband exactly; however, the agreement is close, as shown in S9 Fig. The parameters for C^2 and C^3 were fit similarly. (B) The C^1 , C^2 , and C^3 parameters for the simulation of responses in a V2 electrode for 9 stimuli (8 contrast patterns plus a blank condition). These parameter fits were made using the full ECoG dataset (for this electrode), so there are no error bars on the input parameters. (Code to reproduce this figure can be found on https://github.com/dorahermes/Paper_Hermes_2017_PLOSbiology function ns_script06B_Fig6.m).

<https://doi.org/10.1371/journal.pbio.2001461.g006>

values are not reproduced exactly because the simulations are stochastic, but overall, the original broadband, gamma, and alpha values are recovered with high accuracy (S9 Fig).

As described above, the fitting of the parameters for C^1 , C^2 , and C^3 was constrained by the assumptions that for C^1 , the correlation between neurons was 0 (and the amplitude was varied for fitting); for C^2 , the amplitude was fixed at a nonzero value (and the correlation was varied for fitting); and for C^3 , the correlation was fixed at a nonzero value (and the amplitude was varied for fitting). Results from alternative models with different constraints show poorer fits and are described briefly below and more extensively in S7 Fig.

Importantly, the parameter fits did not take into account the measured BOLD responses. Hence the simulations provided a test: if the input parameters were chosen to produce outputs that match the measured ECoG responses (training data), does the simulated BOLD signal accurately predict the measured BOLD signal (test data)? We measured BOLD responses in four healthy subjects to the same visual stimuli as used in ECoG (subjects are different from the ECoG subjects) and extracted the signal from regions of interest in visual cortex matched to the previously recorded ECoG electrode locations (S2 Fig and S3 Fig). For an example V1 site, the predicted BOLD signal accurately matched the measured BOLD signal, with 89% of the variance in the measured BOLD signal explained by the prediction, as quantified by R^2 —the coefficient of determination (Fig 7A). Across V1 sites, the predicted BOLD signal from the simulations accounted for a median of 80% of the variance in the measured data (Fig 7C). For an example V2 site, the predicted BOLD signal also matched the measured BOLD signal ($R^2 = 0.74$, Fig 7B). Across V2/V3 sites the simulations explained a median of 40% of the variance in the data. The explained variance in V2/V3 is substantial but lower than in V1. One likely reason for the higher variance explained in V1 is that for the particular stimuli used in these experiments (gratings and noise patterns), the BOLD response reliability was higher in V1. For example, the median R^2 computed by using half the BOLD data as a predictor for the other half (split half by subjects) was 86% for V1 and 63% for V2/V3. Similarly, the stimulus-evoked BOLD responses in V1 were larger than in V2 and V3, with more stimulus-related variance to explain: a mean of 1.8% signal change in V1 versus 1.2% in V2 and 0.8% in V3 (S4 Fig). It is possible that a stimulus set more tailored to extrastriate areas, such as textures or more naturalistic scenes, would have evoked more reliable responses in extrastriate cortex.

For each of the 22 simulations, the three input parameters C^1 , C^2 , and C^3 defining each of the 8 stimulus conditions were fit to produce the LFP data from the corresponding ECoG electrode. By design, the C^1 (broadband) and C^3 (alpha) inputs were fit to ECoG data by varying the **level** per neuron, whereas C^2 was fit to data by varying the **correlation** across neurons. In principle, for any of the three inputs, the ECoG data could have been fit by varying either the level per neuron or correlation across neurons. For completeness, we tested all 8 combinations of models (S7 Fig). The most accurate model, quantified as the R^2 between the measured BOLD and the simulated BOLD (median across the sites in V1 or in V2/V3), was the simulation type used in the main text, in which C^1 and C^3 varied in the level per neuron and C^2 varied in the correlation across neurons. Models in which the broadband correlation rather than level was used to fit the ECoG broadband power were much less accurate. The models in which the gamma LFP power was fit by modulating the level rather than the correlation in the simulated population caused a small drop in R^2 .

2.4 Relation between ECoG and BOLD in simulation and data

The previous analysis showed that when simulations were fit to ECoG data, the simulated BOLD response predicted the measured BOLD response. Here, we used regression analyses to assess how the simulated LFP predicted the simulated BOLD response and how the measured LFP predicted the measured BOLD response.

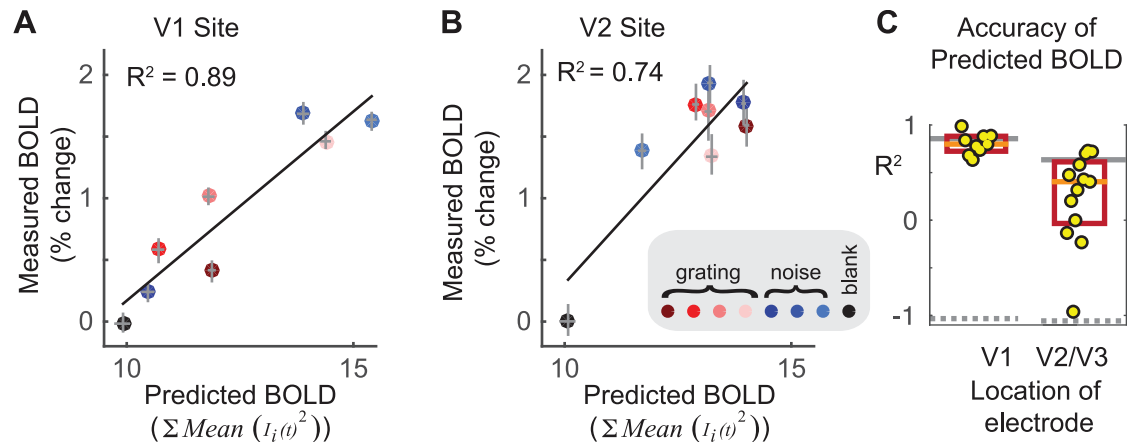


Fig 7. Accuracy of predicted blood-oxygen-level dependent (BOLD) signals from simulated neuronal activity. (A) Simulated BOLD (*x*-axis) versus measured BOLD (*y*-axis) for a V1 site. Each color corresponds to one stimulus condition (red dots, grating patterns; blue dots, noise patterns; black dot, uniform stimulus, or blank). Error bars indicate 68% confidence intervals, bootstrapped 100 times over 30 trials per stimulus for simulation and over repeated scans for BOLD data. (B) The same as A but for a V2 site. (C) The accuracy of BOLD predictions for all V1 and V2/V3 sites. Each site is indicated by a yellow dot. The orange lines show the medians and the red boxes the 0.25 and 0.75 quantiles. The thin, gray, solid lines show the BOLD data-to-data reliability, and the gray dashed lines show the accuracy when the BOLD data and trial conditions are shuffled in the training dataset. Accuracy is quantified as the coefficient of determination after subtracting the mean from the data and the predictions, and dividing each variable by its vector length. Because the simulations were fit to electrocorticographic (ECoG) data and tested on BOLD data, the predictions are cross-validated, and the coefficient of determination spans $(-\infty, 1]$. A value of -1 is expected when the data and predictions are unrelated and have equal variance, as in the case of the shuffled control analysis. (Code to reproduce this figure can be found on https://github.com/dorahermes/Paper_Hermes_2017_PLOSbiology function ns_script07.m).

<https://doi.org/10.1371/journal.pbio.2001461.g007>

2.4.1 Examples of the relation between the BOLD amplitude and LFP features. We first consider an example V1 site (Fig 8A: same site plotted in Fig 7A). The BOLD amplitude for the different stimuli was accurately predicted by the broadband response ($R^2 = 0.85$) but not by the narrowband gamma or alpha power ($R^2 = -0.06$, $R^2 = -0.07$, respectively). Hence, in V1, only broadband power was a good predictor of BOLD amplitude (indicated by the black outlines in Fig 8). Because there were only 8 data points to fit in each of the 3 correlations, we used cross-validation to avoid overfitting: linear regression was used to fit the BOLD signal to the ECoG measure in separate halves of the data, and the R^2 was computed from the left out half of each dataset.

A different pattern was found in the V2/V3 data. For an example V2 site (Fig 8B: same site plotted in Fig 7B), the broadband power did not predict the BOLD signal as accurately as it did for the V1 site ($R^2 = 0.31$), whereas the alpha power predicted the BOLD signal more accurately than it did for the V1 site ($R^2 = 0.59$). Gamma power did not predict the BOLD signal, similar to the V1 data.

For the simulation fit to the ECoG data from the example V1 electrode, the relation between the BOLD signal and the LFP (Fig 8C) was similar to the measured V1 data: the LFP broadband response predicted the BOLD signal ($R^2 = 0.89$), whereas the power of narrowband gamma oscillations and alpha oscillations did not ($R^2 = 0.01$). In this simulation, similar to the data, the LFP broadband response was the only good predictor of the BOLD signal. Hence, the data and the simulation match in that they both show that some features of the LFP are good predictors of BOLD (broadband), and some are poor predictors (alpha and gamma).

For the simulation fit to the ECoG data from the example V2 electrode, the relation between the BOLD signal and the LFP (Fig 8D) was similar to the measured V2 data. First, the broadband LFP was again a good predictor of the BOLD signal, and gamma power was again a poor

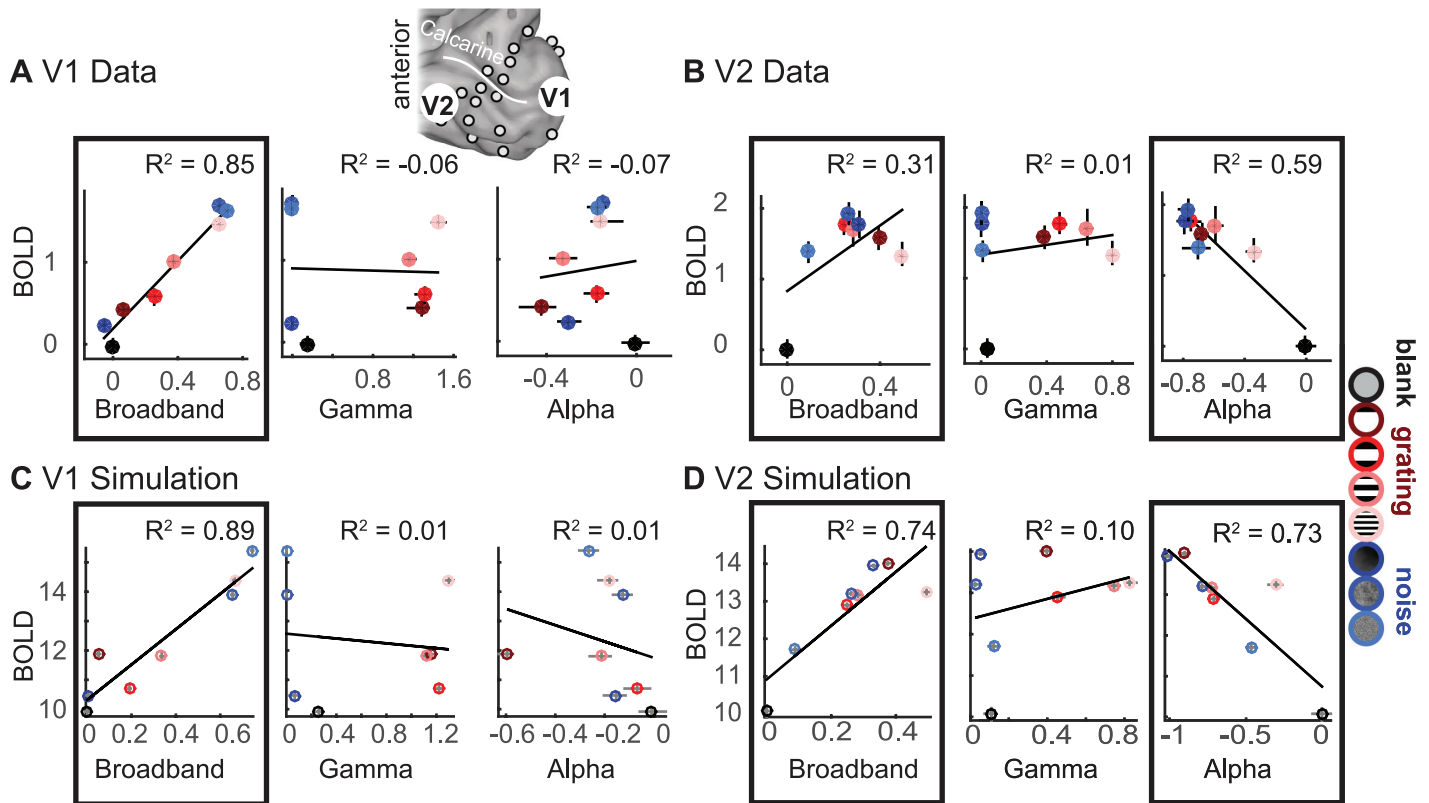


Fig 8. The accuracy of predicted blood-oxygen-level dependent (BOLD) signals from electrocorticographic (ECoG) components. The correlation between ECoG and BOLD was calculated for a V1 site and a V2 site. The locations of one sample electrode in V1 and one in V2 are indicated by the enlarged white discs on the cortical surface for subject 1. (A) In a foveal V1 site, the broadband ECoG amplitude accurately predicted the BOLD signal (left). Error bars show 68% confidence intervals across bootstraps. Narrowband gamma power (center) and alpha power (right) were uncorrelated with BOLD. (B) In a V2 site, the broadband ECoG was weakly correlated with BOLD (left). Narrowband gamma did not predict BOLD (middle). Alpha was negatively correlated with BOLD (right). Scatter plots for all other V1 and V2/V3 sites are shown in S5 Fig. (C-D) The same as A and B but for simulated neuronal population data fit to the V1 and V2 ECoG data. For all panels: data points are the bootstrapped median across 30 trials per stimulus (ECoG) and across scans (BOLD). The trend lines are least square fits to the 8 data points plotted. The R^2 values are the coefficient of determination computed by cross-validation, with a regression fit to half the data and evaluated on the other half. The black outlines indicate the regressions that show reliable predictors of the BOLD signal—broadband in V1, broadband and alpha in V2/V3. (Code to download data and reproduce this figure can be found on https://github.com/dorahermes/Paper_Hermes_2017_PLOSbiology_function_ns_script09A_Fig8AB_Fig9AB.m and function ns_script07B_Fig7AB_Fig8CD.m).

<https://doi.org/10.1371/journal.pbio.2001461.g008>

predictor. Second, the power of alpha oscillations had a strong negative correlation with BOLD ($R^2 = 0.73$).

In the simulations, the correlation between broadband and BOLD is higher for V1 than for V2, and the correlation between alpha and BOLD is higher for V2 than for V1. These differences were not due to a difference in the types of inputs (C^1 , C^2 , C^3), nor to the way BOLD or LFP was derived from the population activity—the simulation algorithm and the analysis code were identical for all simulations. The difference arises only from the different parameters—that is, there were different mixtures of C^1 , C^2 , and C^3 for the V1 and the V2 simulations. This highlights the fact that the identical mechanism converting neural activity to BOLD (“neurovascular coupling”), modeled here as power in the time series summed across neurons (Eq 3), can produce very different correlations between BOLD and features of the LFP, depending on the neural activity.

2.4.2 The relation between the BOLD amplitude and LFP features across sites. In the example V1 site and the corresponding simulation, the BOLD signal was well predicted by

broadband increases (Fig 8B and 8D). In the example V2 site and the corresponding simulation, the BOLD signal was predicted by both broadband increases and alpha decreases (Fig 8C and 8E). By explicitly modeling both the population response and the population-to-instrument transformations, we see that a difference in the relation between instrument measures (BOLD and ECoG) can arise from a difference in the population response, without a difference in neurovascular coupling. We now ask (1) whether these effects are consistent across the measured V1 and V2/V3 sites and (2) how a multiple regression model using broadband, gamma, and alpha as predictors fits the BOLD response for both data and simulation.

As we argued in the Introduction, we believe there is no single, general transfer function that can predict the BOLD signal from the LFP. Yet a regression model linking the two measures can be a useful way to summarize the results of a particular experiment/simulation and to compare results between different experiments/simulations. Here, we fit several regression models to each simulation and to the data (Fig 9). The regression models predicted the simulated or measured BOLD response from either a single LFP component (broadband power, gamma power, or alpha power) or from combinations of LFP components (each of the pairwise combinations, and the three components together). These regression models were fit separately for each of the 9 sites in V1 and each of the 13 sites in V2/V3 and for the 22 corresponding simulations. The accuracy of each model was assessed by the variance explained in the cross-validated data (R^2 , the coefficient of determination). With a cross-validation procedure, there is no advantage in accuracy for models with more free parameters, and accuracy is reduced rather than increased by overfitting. The cross-validated R^2 was compared to the R^2 in a null distribution, derived from shuffling the assignment between data and stimulus conditions.

Data. The single-parameter regression models across V1 electrodes (Fig 9A) show the same pattern as the single electrode examples in Fig 8: broadband alone was a good predictor of BOLD (median cross-validated $R^2 = 0.70$ across 9 sites), while gamma and alpha alone were not (gamma $R^2 = 0.04$, alpha $R^2 = 0.04$). Across all regression models, the observed BOLD signal was best predicted by a combination of broadband and alpha changes with an $R^2 = 0.78$, close to the data-to-data reliability ($R^2 = 0.82$). Adding gamma as a predictor to either the broadband-only model (model 2 versus model 1) or to the combined broadband and alpha model (model 7 versus model 5) did not increase model accuracy, confirming that the gamma amplitude was not predictive of the BOLD signal.

The single-parameter regression models across V2/V3 sites (Fig 9B) show that alpha power predicted the BOLD signal ($R^2 = 0.32$, with a negative Beta value), whereas broadband alone was only slightly more accurate than a control, shuffled model, and gamma alone had no predictive power. As in V1, the BOLD response was best explained by a regression model combining broadband and alpha ($R^2 = 0.39$; see also S6 Fig) or a model using all three predictors ($R^2 = 0.42$). Overall, compared to V1, the BOLD signal in V2/V3 was less accurately predicted by the regression models based on the electrophysiological measurements. As with the case of predicting BOLD from simulated neuronal activity, predicting BOLD from ECoG measures is limited by the reliability of the stimulus-evoked BOLD signal, which was lower for V2/V3 than for V1 (0.59 versus 0.82 R^2).

Simulations. For the simulations, we expect broadband power to positively predict the BOLD signal and alpha power to negatively predict the BOLD signal because of the construction of the simulations: broadband and alpha power elevations were achieved by increasing the variance per neuron, rather than correlations between neurons; the converse was true for gamma. Nonetheless, solving the regression models can be informative because, as seen in Fig 8, simulations with the identical input types and the identical analysis can lead to different patterns, depending on the parameters (weights) in the simulations. Moreover, the regression

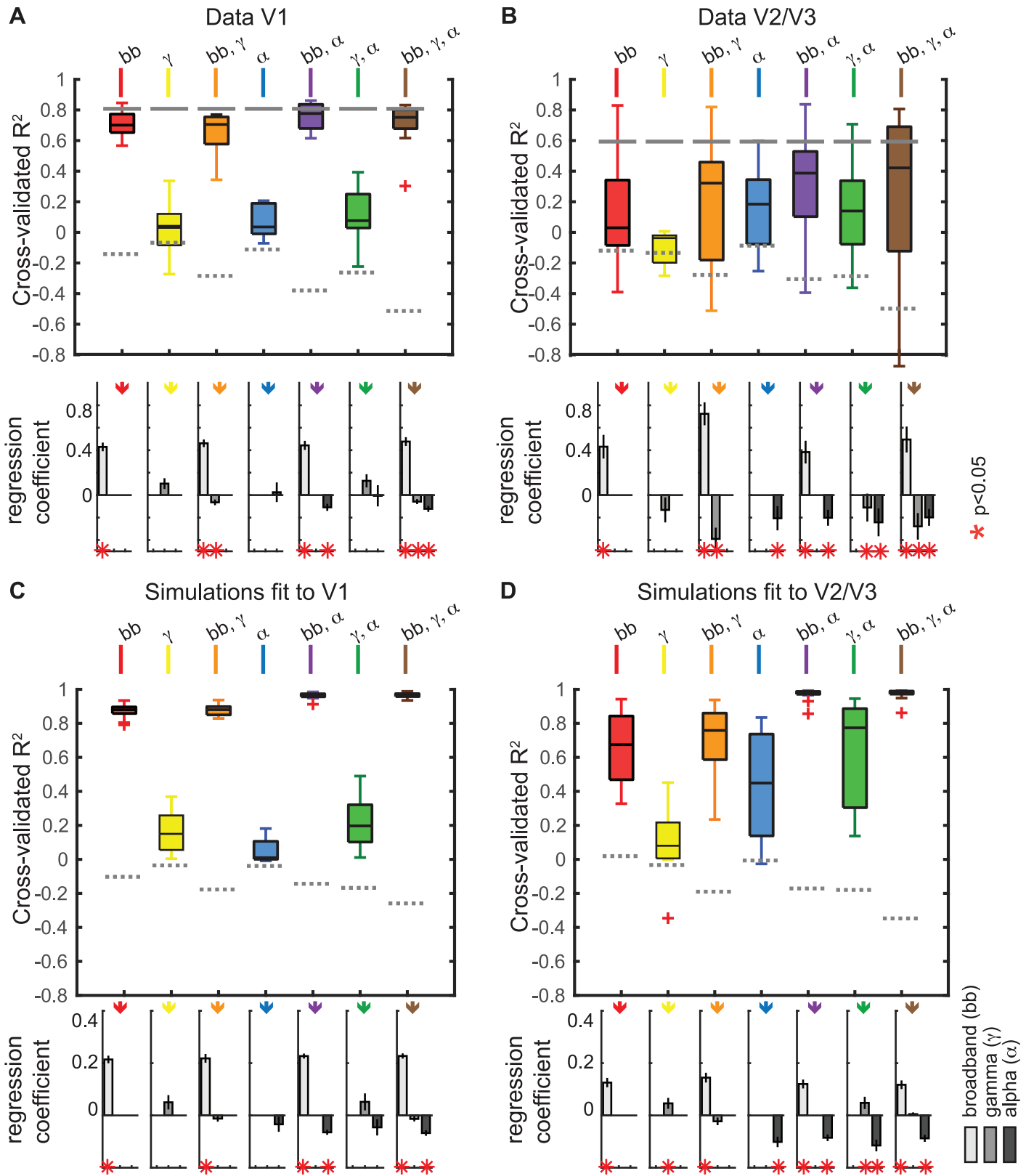


Fig 9. Explained variance in the blood-oxygen-level dependent (BOLD) functional magnetic resonance imaging (fMRI) signal in the simulations and in data. (A) Variance in the measured BOLD signal explained by broadband, gamma, and alpha changes in the electrocorticographic

(ECoG) data. The colored box plots show the variance explained by each of the 7 model types: black bar = median, upper and lower boxes = quartiles, and error bars = data range excluding outliers (outliers plotted as red plusses). The R^2 was cross-validated (split between subjects for BOLD and stimulus repetitions for ECoG) to ensure that the R^2 can be compared between models with different numbers of explanatory variables. Gray dashed lines indicate the noise floor (R^2 when shuffling the BOLD labels in the training data), and the solid gray lines indicate the data-to-data reliability for the BOLD signal. Bottom: the regression coefficients show whether the broadband, gamma, and alpha signals were positive or negative predictors of the BOLD signal. A red * in the lower plot indicates whether regression coefficients differed significantly from 0 by a bootstrap test ($p < 0.05$). (B) The same as A but for the 13 V2/V3 electrodes. (C) The same as A but for the 9 simulations fitted to V1 data. The R^2 was cross-validated (split between even and odd stimulus repetitions). (D) Same as C, except for the 13 simulations fitted to the V2/V3 data. (Code to download data and reproduce this figure can be found on https://github.com/dorahermes/Paper_Hermes_2017_PLOSbiology).

<https://doi.org/10.1371/journal.pbio.2001461.g009>

analyses of the simulated data can be compared against the regression analyses of the measured data.

The results from the regression model on simulated V1 LFP and BOLD (Fig 9C) were qualitatively similar to the V1 data: broadband alone was a good predictor of BOLD (median cross-validated $R^2 = 0.70$ across 9 simulations), while gamma and alpha alone were not (median $R^2 = 0.04$ for both predictors). For simulations fit to V2/V3 ECoG data (Fig 9D), alpha alone predicted the BOLD signal with moderate accuracy (median $R^2 = 0.32$).

Similar to the data, the BOLD response in the simulations fit to V1 and V2/V3 was well explained by a regression model combining broadband and alpha ($R^2 = 0.78$, $R^2 = 0.39$, Fig 9C and 9D). The regression coefficients for these models were positive for broadband and negative for alpha. A model that incorporated all three LFP measures—broadband, alpha, and gamma—explained little to no additional variance for either simulation, confirming our earlier observation that narrowband gamma power was not correlated with BOLD amplitude in simulated data. The generally higher variance explained in V1 than in V2/V3 again matches the higher BOLD reliability in V1 for these experiments.

Across simulations and datasets, a general pattern emerges. The broadband signal was positively predictive of BOLD, and alpha power was negatively predictive of BOLD. Narrowband gamma had no consistent relation with BOLD. While the relationships between broadband and BOLD and between alpha power and BOLD were consistent in terms of sign (the former positive, the latter negative), the level was not always the same. As we noted in the example sites shown in Fig 8, and the summary across sites in Fig 9, the broadband power was more strongly predictive of BOLD in V1, and alpha power was more strongly predictive in V2/V3. An examination of responses to the different stimulus types clarifies the difference between V1 and V2/V3 in these data. Specifically, the BOLD response in V2/V3 to noise patterns was underpredicted by the broadband response alone (S5 Fig). In V2/V3, alpha decreased more for the noise patterns, and this alpha decrease accounted for the BOLD change unexplained by broadband (S1 Fig). This helps to explain why a model that includes broadband and alpha is much more accurate for V2/V3 than a model that includes only broadband. In contrast, for V1, the BOLD response was well predicted by broadband power in most sites, with little systematic prediction failures and little room for increased model accuracy when adding predictors such as alpha power.

2.4.3 Correlation between BOLD and LFP across all frequencies. In the previous section, we modeled the BOLD responses as a linear function of three components derived from the LFP. These features—broadband power, narrowband gamma power, and narrowband alpha power—are summary metrics of the power spectrum. We also tested how the power at each frequency in the ECoG data and in the simulated LFP correlated with the BOLD response (measured and simulated, Fig 10).

Data. We calculated ECoG power for each frequency from 1 Hz to 200 Hz and correlated the power changes from baseline with BOLD changes from baseline. In V1, ECoG responses across all frequencies except the alpha band were positively correlated with the BOLD response

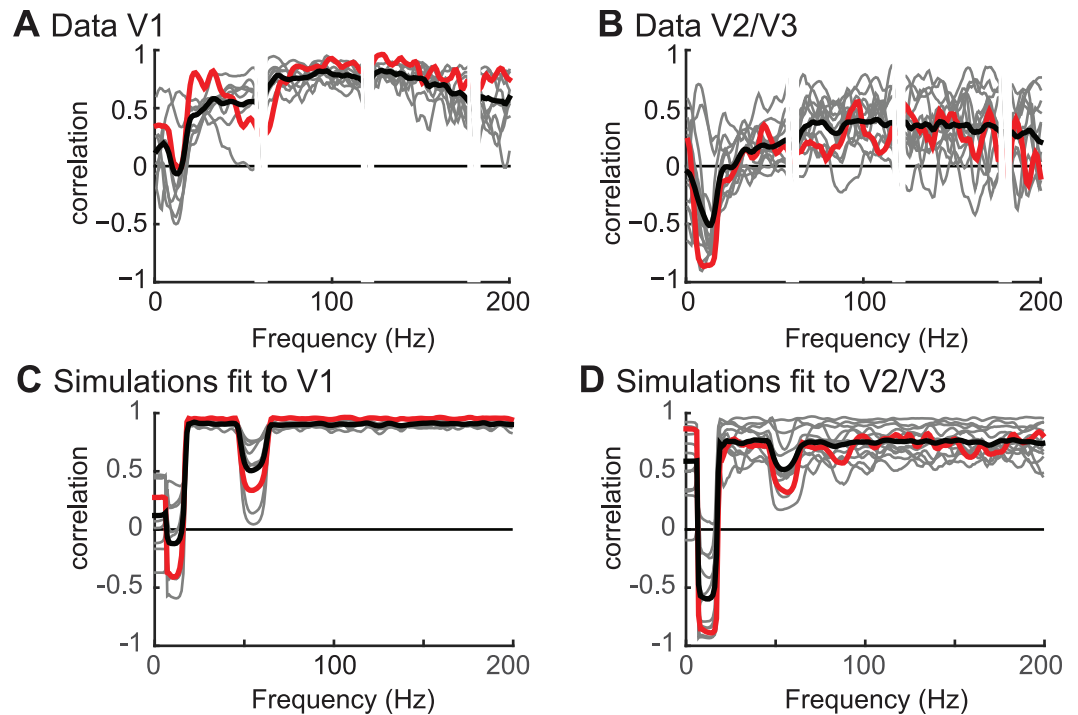


Fig 10. The correlation between blood-oxygen-level dependent (BOLD) and local field potential (LFP) as a function of frequency. (A) The correlation between electrocorticographic (ECoG) and BOLD for the V1 data shows a positive correlation between ECoG and BOLD for a broad range of frequencies, except those including the alpha changes. Gray lines represent the 9 individual V1 electrodes, the black line is the average, and the red line corresponds to the example sites shown also in Fig 7. (B) In the V2/V3 data, there was a strong negative correlation between ECoG and BOLD in the alpha range around 10 Hz and a positive correlation between ECoG and BOLD for a broad range of frequencies. Gray lines represent the 13 individual V2/V3 electrodes, the black line is the average, and the red line corresponds to the example electrode shown also in Fig 7. Note that neither the V1 electrodes nor the V2/V3 electrodes show a peak at the gamma frequency. (C) The correlation between LFP and BOLD for simulations fit to V1 shows that there is a positive correlation across most frequencies, except those including the alpha and gamma changes. (D) The correlation between LFP and BOLD for the simulations fit to V2/V3 shows that there is a strong negative correlation around 10 Hz and a positive correlation across a broad range of frequencies. (Code to download data and reproduce this figure can be found on https://github.com/dorahermes/Paper_Hermes_2017_PLOSbiology_function_ns_script10_Fig10.m).

<https://doi.org/10.1371/journal.pbio.2001461.g010>

(Fig 10), which is consistent with the regression analyses of the summary metrics, showing that broadband ECoG power was the best predictor of the BOLD signal.

The pattern of correlation between ECoG power and BOLD in V2/V3 was similar to that found in V1, although the overall level of correlation was lower (Fig 10). There were positive correlations between ECoG and BOLD extending across most frequencies that were weaker than in V1, and there was a negative correlation for most sites in the alpha band.

Simulation. The correlation between simulated BOLD and ECoG power in V1 was qualitatively similar to that found in the data. In simulations fit to V1 ECoG data, the LFP correlated well with the BOLD signal across all frequencies except those in the alpha band (8 Hz to 15 Hz) and below, and those in the gamma band (40 Hz to 60Hz).

In simulations fit to V2/V3 ECoG data, the pattern was similar, except that the correlation was negative in the alpha band rather than 0, and weaker but still positive in the rest of the spectrum. These patterns match the summary metrics of alpha, gamma, and broadband shown in Fig 9.

Site to site differences. There were some differences between V1 sites. For example, in two sites, the correlation across frequencies dipped in the gamma band (30–80Hz), similar to simulated data. These are also the two sites that showed the largest amplitude gamma responses (sites 8 and 9 in [S5 Fig](#)). In other words, when cortical sites showed large gamma signals, these signals were uncorrelated with BOLD. The fact that in 7 V1 sites there was a positive correlation between BOLD and LFP power spanning 30 Hz to 80 Hz might seem inconsistent with our earlier observation that narrowband gamma power was not predictive of the BOLD signal in V1 sites ([Fig 8](#) and [Fig 9](#)). However, in this analysis, the narrowband and broadband power are not modeled separately, and the positive correlation between power at 30 Hz to 80 Hz in [Fig 10](#) thus likely suggests that broadband power extends into this band, since broadband changes can extend across all frequencies [11, 40]. Therefore, if there is little to no narrowband response, we would expect a positive correlation between BOLD and ECoG throughout all frequencies.

There were some site-to-site differences in the correlation between alpha and BOLD. For example, some sites showed a positive correlation with BOLD in the alpha range, and others showed a negative correlation ([Fig 10A](#) and [10B](#)). These site-to-site differences depend on the range of responses evoked by stimuli. For example, for electrodes in which stimuli evoked a large range of power changes in the alpha band, alpha was more strongly correlated with BOLD. Similarly, for electrodes in which stimuli evoked a large range of broadband responses, broadband was more highly correlated with BOLD ([S8 Fig](#)). This pattern did not hold for narrowband gamma power changes.

Discussion

This study investigated the relationship between electrophysiological and BOLD measurements in human visual cortex. Our modeling framework decomposed the signals into two stages, a first stage in which we simulated the neuronal population responses (dendritic time series), and a second stage in which we modeled the transfer of the neuronal time series to the BOLD signal and the field potential. This approach differs from the direct comparison of electrophysiological signals and BOLD. The explicit separation into stages clarified both a similarity and a difference between the BOLD amplitude and the field potential power: the two can be approximated as the same operations on the neuronal population activity, but applied in a different order. Specifically, within a brief window, we modeled the BOLD amplitude as the sum of the power in the neuronal time series and the field potential as the power of the sum of the neuronal time series. Because the order of operations differs, the two signals differ, and each is blind to particular distinctions in the neuronal activity. For example, the BOLD signal (according to our model) does not distinguish between synchronous and asynchronous neural signals with the same total level of activity. In contrast, the field potential does not distinguish counterphase responses from no response. Even if one knew the exact mechanism of neurovascular coupling and the precise antenna function of an electrode, one still could not predict the relationship between the BOLD signal and the field potential without specifying the neuronal population activity that caused both. Hence, the relationship between the two types of signals is not fixed but rather depends on the structure of the underlying responses of the neuronal population.

Although we do not have access to the complete set of individual neuronal responses in any of our experiments in visual cortex, we approximated the responses by specifying the type of signals common to visual cortex. We therefore limited the space of neuronal population responses by modeling the activity as arising from three types of signals, enabling us to compute the complete set of field potentials and BOLD responses to a variety of conditions. Finally, we compared

the simulated patterns of BOLD and field potential responses to the actual responses we observed in data from human subjects. These patterns are discussed and interpreted below.

3.1 Changes in broadband power predict BOLD

Many studies have reported correlations between BOLD and power in the gamma band LFP (30–130 Hz) (review for human studies: [52]). Yet, changes in gamma band power do not reflect a single biological mechanism. For example, several recent studies have emphasized that LFP power changes in the gamma band reflect multiple distinct neural sources, including narrowband oscillations and broadband power shifts, with very different stimulus selectivity and biological origins [38, 53, 54].

Broadband changes have been proposed to reflect, approximately, the total level of Poisson-distributed spiking (or spike arrivals) in a local patch of cortex [40]. In contrast, the narrowband gamma response is caused by neural activity with a high level of cell-to-cell synchrony [55] and likely depends on specialized circuitry [56]. While the two responses are sometimes distinguished as “high gamma” (referring to broadband signals) and “low gamma” (referring to oscillatory signals), this distinction is not general. Broadband signals can extend into low frequencies [11, 57] so that the two signals can overlap in frequency bands. Hence, separating gamma band field potentials into an oscillatory component and a broadband (nonoscillatory) component is not reliably accomplished by binning the signals into two temporal frequency bands, one low and one high, but rather requires a model-based analysis, such as fitting the spectrum as the sum of a baseline power law (to capture the broadband component) and a log-Gaussian bump (to capture the oscillatory component) [38].

There is strong experimental support for the idea that increases in broadband LFP power primarily reflect increases in asynchronous neural activity rather than increases in coherence. First, experiments have shown that broadband power is correlated with multiunit spiking activity [54, 58]. Second, unlike the case of narrowband gamma LFP, changes in broadband LFP are not accompanied by changes in broadband spike-field coupling (Figure 1A-B in [43]). The possibility that neuronal synchrony sometimes affects broadband signals cannot be ruled out, for example, as shown in cases of pharmacological manipulations in nonhuman primates [59]. In such cases, there would not be a simple relationship between broadband power and BOLD.

The prior literature has not shown definitively whether broadband LFP, narrowband gamma, or both predict the BOLD signal. The first study that directly compared simultaneously recorded BOLD and electrophysiology showed that both LFP power in the gamma frequency range (40–130 Hz) and multiunit spiking activity (MUA) predicted the BOLD signal [16] and further, that when the LFP power diverged from MUA, the gamma band LFP predicted the BOLD signal more accurately than did spiking. This study however did not separately test whether a narrowband (oscillatory) or a broadband (nonoscillatory) component of the LFP better predicted the BOLD response.

Other studies, too, have shown a variety of patterns when correlating LFP power changes in the gamma band with BOLD. Some reported that BOLD amplitude correlates with narrowband gamma activity [13], while others showed that BOLD correlates with broadband changes [11], and many did not distinguish narrowband from broadband power in the gamma band [60]. Simultaneous recordings of hemodynamic and neuronal activity in macaque V1 showed that BOLD signals from intrinsic optical images can occur in the absence of gamma band LFP changes [61] and that, in some circumstances, multiunit activity predicts the BOLD signal more accurately than gamma band LFP [24, 62].

Here, we separately quantified the broadband power (spanning at least 50–150 Hz) and narrowband gamma power. We found that the amplitude of broadband changes accurately

predicted the BOLD signal in V1. The empirical results and the models help resolve the question of why “high gamma” has been shown to correlate with BOLD, and “low gamma” sometimes does not [24]. The likely reason is unrelated to the difference in frequency range, nor to the size of the spectral perturbation in the LFP. In fact, the elevation in broadband power is relatively small (2- or 3-fold) compared to the elevation in power often observed in narrowband gamma oscillations (10x or more)[38]. Instead, “high gamma” is predictive of the BOLD signal in many cases not because of the specific frequency range, but because this signal captures the level of asynchronous neuronal response; this signal happens to be most clearly visible in the high-frequency range (>100 Hz) in which it is not masked by rhythmic lower-frequency responses. Hence, the distinction in predicting the BOLD response is not about “high” versus “low” gamma but rather synchronous versus asynchronous responses, and the broadband signal, sometimes labeled high gamma, maps onto the first term on the right-hand side of Eq 4, the portion of the field potential measurement that sums the energy demand of each neuron.

Our model fits and data support this view. When we captured the stimulus-related broadband response by simulating a change in broadband coherence across neurons rather than a change in the level of response in each neuron, our predicted BOLD response was highly inaccurate (S7 Fig).

3.2 Changes in narrowband gamma power do not predict BOLD

In contrast, we propose that “low gamma” often does not predict the BOLD response because “low gamma” reflects narrowband oscillatory processes, which largely arise from a change in neuronal synchrony across the population rather than a change in the response level per neuron. This corresponds to the second term in the right-hand side of Eq 4, the portion of the field potential measurement that reflects the cross-power arising from currents in different neurons, which in our model, is independent of the signals giving rise to the BOLD signal.

Our results and model do not argue that narrowband gamma oscillations will never be predictive of the BOLD signal. If, in a particular experiment, narrowband gamma oscillations were to covary with broadband increases, we would expect both signals to correlate with BOLD. This might occur in an experiment with gratings of different contrast; with increasing contrast, narrowband gamma responses, broadband responses, and BOLD responses all increase [21, 63], and all three measures would correlate across stimuli. In such an experiment, if narrowband gamma oscillations had a higher signal-to-noise ratio than the broadband response, then the oscillatory signal would likely show a higher correlation with BOLD. In contrast, when the choice of stimulus or task can independently modulate broadband power and gamma oscillations so that the two LFP measures are not correlated, as in the experiments presented here and previously [38], then gamma oscillations will not strongly correlate with BOLD.

Our simulation and empirical results are consistent with studies that varied chromatic contrast and spatial frequency while measuring MEG and BOLD. These studies found that BOLD and narrowband gamma activity did not match in stimulus specificity [18, 19]. It is likely that these stimulus manipulations, like ours, independently modulated narrowband gamma power and broadband power, although the studies did not quantify broadband fields, which are more challenging to measure with MEG than with ECoG [64]. We speculate that broadband fields spanning the gamma range would have shown a higher correlation with BOLD.

3.3 Neuronal synchrony and the BOLD signal

In our model, the LFP measures are highly sensitive to neuronal synchrony, whereas BOLD is not. In our simulations, increases in neuronal synchrony drove narrowband gamma oscillations in the field potential. There are other cases of population activity with a high degree of

neuronal synchrony. One example is the steady-state evoked potential associated with a periodic stimulus [65, 66]. Previous studies have described discrepancies between evoked potentials and the BOLD signal, such as in the case of spatial summation [11], directional motion selectivity [7, 8] and spatial attention [9, 10]. Our modeling framework suggests that the neural sources generating the steady-state potential (synchronous neural activity) are likely to be only weakly related to the BOLD signal (depending largely on asynchronous signals), as these sources will primarily affect the second term on the right-hand side of Eq 4 (cross-power). This does not imply that the two measures are always or even usually discrepant; the BOLD signal and steady-state potentials are likely to correlate any time that the steady state signals correlate with other measures of neural activity. When measures do dissociate, we do not conclude that one measure is more accurate; instead, the measures offer complementary views of the population activity, emphasizing the degree of synchrony or the average level of the response. An intriguing question is how each of the two signals contributes to perception and behavior [67].

Neural synchrony can also emerge without being time-locked to the stimulus, often called “induced synchrony” or “induced oscillations” [68]. In our simulation, we assumed that narrowband gamma LFP changes were induced by increases in **synchrony** between neurons and not by changes in the **level** of gamma power within the individual neurons. In contrast, we assumed that broadband LFP increases were induced by increased broadband activity in individual neurons and not by increased broadband coherence between neurons. (In Eq 4, a change in the left-hand side, LFP power in the gamma band, can be produced by a change in either the first or second term on the right). This explains why, in our simulation, the broadband power was correlated with BOLD, whereas the LFP gamma power was not, findings that were also confirmed by the data. Were our assumptions justified?

In principle, an increase in narrowband gamma power in the LFP could arise because the neurons synchronize in the gamma band or because ongoing gamma oscillations within each neuron increase in amplitude, independent of coordination between neurons. There is strong experimental support for the former. Experiments that measure both intracellular membrane potential from single neurons and the extracellular LFP show that when there is an increase in narrowband LFP gamma power, the gamma power from individual neurons becomes more coherent with the LFP [47]. Moreover, the coherence between local spiking and the LFP also increases in the gamma band when LFP gamma power increases [43]. These results are consistent with our assumption that a significant part of the increase in gamma LFP power arises from a change in population coherence. To our knowledge, it is not certain whether there is also some increase in the level of gamma signals within individual neurons when the narrowband gamma band LFP power changes. However, since we can attribute a large part of the change in gamma LFP to a change in coherence, we infer that we can only attribute, at most, a small part of the change in gamma LFP to the level of gamma power within neurons.

In our simulation, we made two simple but extreme assumptions. First, we assumed that gamma oscillations occur with no change in the total level of neural activity, and hence no change in metabolic demand or BOLD. Second, we assumed that broadband responses occur with no change in neural synchrony. While these assumptions are likely incorrect at the limit, the simulations nonetheless captured the pattern of ECoG and fMRI results obtained in our datasets. Alternative models in which the broadband response was caused by a change in synchrony were much less accurate (S7 Fig). Models in which gamma responses were caused by a change in level were only slightly less accurate and cannot be ruled out entirely (S7 Fig). However, the regression models fit to our data (Fig 9) show that the power of narrowband gamma oscillations does not predict the BOLD response. Hence the most parsimonious explanation is that these responses in the LFP are caused in large part by changes in synchrony.

3.4 Mean offsets and the BOLD signal

Both our measurements and our simulations showed that broadband electrophysiological responses were related to, but did not fully account for, the BOLD signal. This was especially evident in Simulation 2 and extrastriate data (V2/V3). In these cases, the amplitude of low-frequency oscillations (8–15 Hz) was negatively correlated with the BOLD signal, independent of broadband signals. Numerous previous studies have reported that low-frequency oscillations are anticorrelated with BOLD, including measurements in motor, visual, and language areas [20–22, 69–71]. This result may appear to conflict with the prior discussion, since we argued that oscillations (to the degree that they reflect neuronal synchrony) should have little to no effect on metabolic demand or the BOLD signal. It is therefore important to ask why low-frequency oscillations sometimes correlate with the BOLD signal, both in data and in simulation.

One explanation is that alpha oscillations, or a mechanism that generates the oscillations, affect the BOLD signal indirectly by inhibiting cortical activity. According to this explanation, an increase in alpha power results in a decrease in local spiking activity, in turn reducing metabolic demand and the BOLD signal [72]. Alpha oscillations may indeed co-occur with reduced cortical excitation [73]. However, if this coupling between alpha power and spiking was the only explanation for the relationship between alpha power and BOLD, then a more direct measure of neuronal excitation, such as broadband or multiunit activity, would adequately predict the BOLD signal; alpha power would negatively correlate with the BOLD signal but would provide no **additional** predictive power. Our data and model do not support this explanation, as we find that for most cortical sites, the most accurate predictor of the BOLD signal is a combined model including both the amplitude of alpha oscillations and broadband power.

We therefore propose that in addition to the indirect effect of modulating cortical excitability, alpha oscillations are also accompanied by a mean shift in membrane potential, making it less depolarized (i.e., closer to the equilibrium potential), and this shift reduces metabolic demand. Indirect evidence for a mean shift comes from MEG and ECoG studies [49, 50, 74], which refer to alpha oscillations as being asymmetrical (i.e., they are not centered at 0—there is a mean shift). This can be explained by a simple process: if alpha oscillations reflect periodic inhibitory pulses, then on average, they will cause a hyperpolarization (or less depolarization). If the neuron was slightly depolarized before the inhibitory alpha pulses, then the pulses would push the neuron toward equilibrium and hence a lower-energy state. In this view, large alpha oscillations reflect larger inhibitory pulses, reducing depolarization. We suggest that this reduced depolarization affects metabolic demand in two ways: by reducing spiking (as discussed above) and by maintaining a less-depolarized state, reducing metabolic demand. In our model, the contribution to the BOLD signal from each neuron is the power in the time series (Eq 3), and the mean contributes to power. The idea that a mean shift in the membrane potential affects metabolic demand (in addition to altering excitability) is consistent with the observation that slowly changing currents (<0.5 Hz) correlate with BOLD fluctuations [12, 75]. Moreover, if alpha oscillations are associated with a mean shift in membrane potential, this would explain why cortical excitability depends on the phase of the alpha cycle: at one phase, the membrane potential is more depolarized, and hence cortex is more excitable, and in the opposite phase, cortex is more hyperpolarized and hence less excitable. This is consistent with the observations that the threshold for eliciting a phosphene with TMS changes with alpha phase [76, 77] and that the alpha phase at the time of stimulus presentation influences the size of the BOLD response in visual cortex [78].

Inhibition takes two neurons—one to inhibit and one to be inhibited. In our simulations, the alpha oscillations (C^3) were associated with inhibitory fluctuations in the membrane potential (mean below 0), which in turn was associated with decreases in BOLD. It is important to

note that these fluctuations are meant to capture the effect of local inhibition on the postsynaptic neurons (the neurons being inhibited). The inhibitory neurons themselves are presynaptic, and the action of inhibiting other neurons is presumably an active process that consumes energy. Therefore, inhibition is expected to increase energy demand in some neurons (the presynaptic neurons) and decrease energy demand in other neurons (postsynaptic neurons). We did not model the inhibitory neurons explicitly; however, the neural activity associated with active inhibition would be expected to contribute to the measured broadband signal in the ECoG data and is implicitly included in the broadband inputs in our simulations (C'). More complex models (see paragraph 3.6) in which the circuitry of excitatory and inhibitory neurons is explicitly represented (such as [63, 79, 80]) may provide insight into how the balance between excitation and inhibition influences the field potential and the BOLD signal.

3.5 A single modeling framework accounts for patterns of LFP/BOLD correlations across sites

We found that the relationship between the BOLD signal and features of the ECoG data differed across cortical areas. For example, broadband changes in ECoG responses explained more variance in the BOLD data in V1 than in V2/V3. Conversely, low-frequency power decreases (alpha, 8–13 Hz) explained more variance in the BOLD signal in V2/V3 than in V1. In the absence of a model, we might have interpreted the results as evidence that neurovascular coupling differs across sites. Many previous studies have reported differences in the relation between LFP and BOLD as a function of site or condition, for example, between cortical and subcortical locations [81], across cortical regions [82, 83], between cortical layers [84], and as a function of medication [85]. Here, we showed that a difference in the relationship between LFP and BOLD need not arise because of a difference in neurovascular coupling. In our results, Simulations 1 and 2, like V1 compared to extrastriate areas, showed differences in the relationship between LFP and BOLD, yet we used the identical model of neurovascular coupling in all simulations. The systematic differences in the two simulations arose because of differences in the neuronal population activity, not because of differences in neurovascular coupling. While our results do not exclude the possibility of differences in neurovascular coupling across locations or states, they do caution against interpreting differences in the relationship between field potentials and BOLD as evidence for a difference in neurovascular coupling, since they show that a single model can account for a variety of patterns. More generally, the V1 versus V2/V3 discrepancies bolster the argument that one cannot predict the exact relationship between BOLD and field potentials without also specifying the neuronal population activity.

3.6 The role of a simple model in understanding the relation between BOLD and LFP

A complete description of the biophysical processes giving rise to the BOLD signal and the field potential is far beyond the scope of this paper and is likely premature given the enormous complexity in the nervous system, the vascular system, and the coupling mechanisms between them. Instead, the purpose of our modeling framework was to first begin with a general principle, namely that BOLD and field potentials sum neural activity according to a different sequence of operations; second, to instantiate this principle in simple mathematical rules; third, to combine these rules with a minimal model of neural population activity; and finally, to ask to what extent such a model can account for the patterns in our data.

Our model omits many biophysical components, such as compartmentalized neurons, multiple cell types and vessel types, neurotransmitters, the dynamics of blood flow, and so on; hence, it is not a detailed simulation of the nervous system or vascular system. We modeled

the BOLD signal as a function of dendritic currents summed across neurons within an imaging region. The logic motivating this is straightforward. Neuronal activity consumes a large amount of energy, and this energy demand is dominated by the cost of restoring the membrane potential following ionic flows from synaptic potentials and action potentials [86, 87]. As a result, the increased energy demand from neuronal responses is related to the dendritic currents. Neurovascular coupling is the process of increasing blood flow to meet this energetic demand; a failure of the hemodynamic response such as stroke can cause neuronal and glial cell death, highlighting the importance of the relationship between blood supply regulation and neuronal activity [33].

We modeled the hemodynamic response as being proportional to the energy demand from dendritic currents. This model was proposed as a computational summary of the approximate relationship between the BOLD signal and neuronal activity, not as a hypothesis about a causal mechanism. Recent work suggests that energy consumption per se (e.g., the change in the cerebral metabolic rate of oxygen consumption) is not the triggering mechanism for the increased blood flow, rather neurotransmitters and other molecules associated with synaptic events are part of a complex cascade that causes vasodilation and changes in blood flow [33, 88, 89]. The exact biological mechanism responsible for neurovascular coupling is an area of highly active, ongoing research [35]. The key assumptions in the model—that the BOLD signal is correlated with changes in membrane potential and that the order of operations differs for the BOLD signal and the LFP—makes accurate predictions for our dataset. A separate and important research question is how closely the biophysical mechanisms match this computational-level description, and what these mechanisms are.

The simplicity of the model has benefits. It facilitates an understanding derived from basic principles, similar to the advantages in building computational, rather than biophysical, models of neural responses [90–93]. Both types of models and empirical studies are valuable. Here, we emphasize that even with a highly simplified model of the BOLD signal, the field potential, and neuronal population activity, we are able to reconcile a wide range of findings in a complicated and technical literature. The model accounts for differences in how broadband field potentials and gamma oscillations relate to the BOLD signal. It can explain differences between cortical areas in the relationship between field potentials and BOLD. The model also provides an explanation for why the amplitude of alpha rhythms is negatively correlated with BOLD, even after accounting for the relationship between broadband signals and BOLD.

We note that drastic simplifications are the norm in many fields of neuroscience, such as receptive field modeling of visual neurons; most such models omit fixational eye movements, optical properties of the eye, retinal and cortical circuitry, etc., instead modeling responses as a few simple mathematical computations of the stimulus (filtering, thresholding, and normalization) [94]. These highly simplified models will certainly fail under some conditions [95], yet they have proven to be of immense value to the field [93], in part due to their simplicity and in part because the alternative in which the responses of visual neurons are computed from a complete, neurobiologically realistic model of the nervous system simply does not exist.

3.7 Reproducible computations

To test competing computational theories about the relation between the visual input, the LFP, and the BOLD response, it is essential to make sample data and code available for others [38, 53]. Following standard practices of reproducible research [96–98], the Matlab code of the simulation and sample data and code to reproduce the Figs in this manuscript can be downloaded at https://github.com/dorahermes/Paper_Hermes_2017_PLOSbiology.

3.8 Conclusions

To understand how the electrophysiology and BOLD responses are related, it is necessary to specify both the manner in which population activity transfers to the two signals and the neuronal population activity itself. The former shows that the covariance between neuronal time series has a large influence on the field potential and not the BOLD signal. Based on our simulations and empirical results, we made several inferences about the neuronal population responses mediating the BOLD signal and the LFP: that narrowband gamma oscillations in visual cortex likely arise more from synchronization of neural responses than a change in level of the neural response and hence have a large influence on the field potential and little influence on the BOLD signal, that responses that are asynchronous across neurons manifest in broadband field potentials and an elevated BOLD signal, and that low-frequency oscillations observed in field potentials are likely accompanied by a widespread hyperpolarization, which in turn reduces metabolic demand and the BOLD signal. Our model-based approach brings us a step closer to a general solution to the question of how neural activity relates to the BOLD signal.

Materials and methods

4.1 Ethics statement

Informed, written consent was obtained from all subjects. The fMRI protocols were approved by the New York University IRB and ECoG protocols were approved by the Stanford University IRB, according to the principles expressed in the [Declaration of Helsinki](#).

4.2 Simulated neuronal time series

Simulations were computed for a population of 200 neurons. Each simulation trial was 1 second long with millisecond sampling. The time series for each neuron was derived by summing three inputs, each 1 second long, followed by leaky integration with a time scale of 10 milliseconds to simulate temporal integration in the dendrite ([Fig 4](#)). Each simulation was fit to ECoG data from one electrode and consisted of 240 trials, 8 repeats of 30 stimulus conditions. A condition in the simulation was defined by the parameter settings for the three inputs ([Fig 4](#)): C^1 (broadband), C^2 (gamma), and C^3 (alpha). Variations in these three inputs resulted in power changes in the broadband, gamma, and alpha LFP. The inputs were fit to data such that the simulated LFP power changes matched the ECoG data power changes for a particular electrode and stimulus.

4.2.1 C^1 —Broadband input. The first input was a series of random numbers drawn from a normal distribution, with no temporal dependencies and no dependencies between neurons.

Motivation. This input approximates spike arrivals with a Poisson distribution at a fixed rate for a given 1-second trial. A random normal distribution was used rather than a Poisson distribution for computational efficiency. (The pattern of results is the same for either distribution.) The input has a flat (white) power spectrum up to the sampling limit of 500 Hz. When coupled with leaky temporal integration (described in a subsequent section), this input results in a power spectrum that is approximately proportional to $1/f^2$ (brown noise). Several groups have proposed that the approximately $1/f^n$ power spectra observed in field potentials arises from white noise (or Poisson noise) input to individual neurons, coupled to one or more low-pass filters [[40](#), [99](#), [100](#)]. Previously proposed sources of filters include an exponentially decaying current response in the synapse following each spike arrival [[99](#)], leaky temporal integration in the dendrite [[40](#)], and frequency dependent propagation in the extracellular tissue [[101](#)], the last of which has since been shown to be unlikely [[102](#)]. Regardless of the source of

the low-pass filtering, the general proposal makes an interesting prediction, namely that a spectrally broadband increase in field potential power in response to a stimulus is likely to indicate an increase in the rate of spike arrivals following that stimulus [40]. This hypothesis has empirical support, based on correlations between spike rates (single-unit and multiunit) and broadband field potentials [54, 58] and the fact that a $1/f^n$ baseline spectrum, as well as stimulus-dependent broadband power increases, can be observed in intracellular (single neuron) membrane potentials in awake macaque visual cortex [42]. This hypothesis is the logic behind our choice to model both the baseline $1/f^n$ spectrum and stimulus-dependent broadband modulations as arising from spectrally flat inputs followed by low-pass filtering within individual neurons. For computational tractability, we explicitly modeled only one of the low-pass filters—leaky integration in the dendrites. We assumed that spectrally broadband signals reflect uncorrelated activity. First, we have shown that the broadband ECoG signal is asynchronous with respect to a visual stimulus and hence uncorrelated from trial to trial [11]. Here, we extrapolate that within a trial, the contribution to the broadband signal is asynchronous from neuron to neuron. One reason to assume so is based on a physiological model: the broadband signal has been hypothesized to arise from the leaky integration of Poisson-distributed spike arrivals [40]. Even if the spike rate is correlated between neurons, the spike timing within a trial is likely to have low correlations between neurons.

Parameters. For each simulation, the Gaussian distribution defining C^1 always had a mean, $\mu = 0.25$. The slightly positive mean ensured that in the baseline state, the membrane potential was slightly positive, such that a suppressive signal (described in the section C^3) could bring the potential closer to 0, hence reducing the metabolic demand. For the 8 conditions in each simulation, the baseline standard deviation of the distribution was set at $\sigma = 0.3$. A larger σ results in a larger broadband signal and can be thought of as reflecting a higher Poisson rate of spike arrivals. The σ for each condition was calibrated such that the resulting changes in broadband power for each of the 8 stimulus conditions matched the changes in broadband power in the ECoG data (Fig 6, see S9 Fig).

4.2.2 C^2 —Narrowband oscillations in the gamma band. The second input was band-passed filtered white noise. The white noise was drawn from a distribution with 0 mean and fixed standard deviation on all trials and for all neurons and subsequently band-pass filtered. Unlike C^1 , there were dependencies (coherence) between neurons. The level of coherence varied across the 8 trial types in each simulation.

Motivation. This input approximates a circuit producing narrowband gamma oscillations in the field potential. Parvalbumin positive interneurons project to pyramidal neurons and can produce fluctuations in the membrane potential of the pyramidal neurons in gamma frequencies from 30–80 Hz [47]. The narrowband rise in gamma power associated with certain stimuli or tasks appears to reflect an increase in synchrony between neurons in this band [103]. Therefore, unlike C^1 , which varied in level but not coherence as a function of condition, C^2 varied in coherence but not level as a function of condition.

Parameters. For all trials and all conditions, the white noise samples were drawn from a normal distribution with $\mu = 0$ and $\sigma = 0.2$. The covariance of the distributions could range between 0 and 1 (using Matlab's `mvrnd` function). The white noise inputs were filtered between 50 Hz and 60 Hz prior to temporal integration in the dendrite: inputs were first zero-padded, then filtered with a 10th order Butterworth filter in forward and reverse direction. (Fig 4). The covariance for each simulation was calibrated such that the resulting changes in narrowband gamma power for each of the 8 stimulus conditions matched the changes in narrowband gamma power in the ECoG data.

4.2.3 C³—Narrowband oscillations in the alpha band. The third input was band-passed filtered white noise, with an added asymmetry such that increased power decreased the mean amplitude. The coherence was the same for all trials and all neurons; the amplitude of the pulses varied by condition.

Motivation. Oscillations in the alpha band (8–15 Hz) are widely observed in visual cortex, with higher amplitudes associated with low sensory stimulation (e.g., eyes closed or zero contrast) or a low-level attention. One model of alpha oscillations is that pyramidal neurons in visual cortex receive pulses of inhibition (hyperpolarizing inputs) spaced on the order of 100 milliseconds, generated indirectly by thalamic-cortical loops [49, 50]. According to this view, less active states are associated with larger inhibitory pulses, resulting in a time-averaged hyperpolarization, compared to more active states with smaller inhibitory pulses. The inhibition is pulsed rather than continuous so that the reduced cortical responsiveness is dependent on the phase of the alpha cycle (most reduced following each inhibitory pulse). Individual neurons in visual cortex can indeed show membrane oscillations at frequencies around 10 Hz [51], indicating that it is reasonable to model the alpha oscillation measured in the population as arising from oscillations in individual neurons, rather than arising only from band-limited coherence between neurons.

Parameters. For all trials and all conditions, the white noise samples were drawn from a normal distribution with $\mu = 0$ and $\sigma = 1$. The covariance of the distributions was fixed at .75 (using Matlab's `mvnrnd` function). The white noise inputs were filtered between 9 Hz and 12 Hz prior to temporal integration in the dendrite: inputs were first zero-padded, then filtered with a 10th order Butterworth filter in forward and reverse direction. The envelope was calculated by a Hilbert transform and added to the signal, and the signal was multiplied by -1 , such that increases in power reduced the mean amplitude. The signal was then multiplied by a factor c_3 , which was calibrated such that the resulting changes in narrowband alpha power for each of the 8 stimulus conditions matched the changes in narrowband alpha power in the ECoG data.

4.2.4 Fitting the LFP power changes to the ECoG power changes. Changing inputs in C^1 , C^2 , and C^3 results in a change in LFP power in broadband, gamma, and alpha, respectively. In order to fit the simulated LFP power changes to the ECoG power changes we quantified the input to LFP output relation, such that a certain change in simulated LFP power could be predicted by change in the input amplitude. Different functions described the relation between the input and LFP. The relation between broadband input and LFP broadband was described as

$$LFP_{broadband} = a \cdot \log_{10} \frac{b + C_1}{b} \tag{Eq 10}$$

Since gamma and alpha were dependent on broadband amplitude (an increase in broadband noise masks the relative contribution of narrowband oscillations), the following function described the relation between input and gamma and alpha LFP:

$$LFP_{gamma} = a \cdot 10^{\frac{-LFP_{broadband}}{m}} \cdot \log_{10} \left(\frac{b + C_2}{b} + c \cdot LFP_{broadband} \right) + d \tag{Eq 11}$$

$$LFP_{alpha} = a \cdot 10^{\frac{-LFP_{broadband}}{m}} \cdot \log_{10} \left(\frac{b + C_3}{b} + c \cdot LFP_{broadband} \right) + d \tag{Eq 12}$$

Parameters a , b , c , d , and m were estimated by a separate calibration procedure in which C^1 , C^2 , and C^3 were systematically varied and LFP broadband, gamma, and alpha were

calculated. **S9 Fig** shows that using this procedure the simulated LFP power changes match the ECoG power changes well.

4.3 Stimuli and task

Stimuli for ECoG experiments were reported previously [38]. In brief, for one subject, the stimuli came from 8 classes of patterns (30 exemplars per class, 20x20°), including high contrast vertical gratings (0.16, 0.33, 0.65, or 1.3 cycles per degree square wave) noise patterns (spectral power distributions of k/f^4 , k/f^2 , and k/f^0), and a blank screen at mean luminance (**S2 Fig**). For the second ECoG subject, there were the same 8 classes as well as two other stimulus classes—a high contrast white noise pattern and a plaid at 0.65 cpd. The fMRI subjects had the same 10 stimulus classes as the second ECoG subject.

4.3.1 ECoG task. ECoG data were re-analyzed from a previous report [38]. We briefly summarize that experiment here. Subjects viewed static images of gratings and noise patterns for 500 ms each, with 500 ms of zero-contrast (mean luminance) between successive stimuli. Order of presentation was randomized (**S2 Fig**). There were a total of 210 contrast stimuli, shown once each in a single, continuous experiment (and 210 interstimulus blanks). Stimuli were shown on a 15-inch MacBook Pro laptop using Psychtoolbox (<http://psychtoolbox.org/>). The laptop was placed 60 cm from the subject's eyes at chest level. Screen resolution was 1280x800 pixels (33x21 cm). Coordinates of the population Receptive Fields (pRF) were obtained from a prior study [11].

4.3.2 fMRI task. The fMRI experiment was a block design, with 12-second stimulus blocks alternating with 12-s blank periods (mean luminance). During the stimulus blocks, images were presented at the same rate as the ECoG experiment: 500 ms duration alternating with 500 ms of zero-contrast (mean luminance) between images (**S2 Fig**). All stimuli from each block came from one of the 7 stimulus classes. The exemplars within the block were all different. Subjects participated in 8 scans of 9 blocks each, and block order was randomized using Latin squares. Two of the fMRI subjects (S2 and S3) additionally participated in an identical experiment using lower contrast images, resulting in similar findings. fMRI subjects participated in two pRF runs to identify retinotopy maps. Stimuli for the pRF experiments consisted of a bar (width = 3 deg) that swept across the visual field in 8 directions: the four cardinal directions and the four diagonals. The bar contained a drifting checkerboard with 100% contrast. Images were projected on a screen in the rear of the magnet bore using an LCD projector (LC-XG250, Eiki) with a resolution of 1024x768 (60 Hz refresh rate) and subtending approximately 32x24 visual degrees (32.4x24.3 cm). Subjects viewed the screen with a mirror mounted to the RF coil. The viewing distance was approximately 58 cm.

4.4 ECoG procedure

ECoG data were measured from two subjects who were implanted with subdural electrodes (2.3 mm diameter, AdTech Medical Instrument Corp) for clinical purposes at Stanford Hospital. Informed, written consent was obtained from all subjects. ECoG protocols were approved by the Stanford University IRB. In 22 electrodes in V1 V2 and V3, broadband and narrowband gamma responses were quantified as before [38], and alpha power changes were calculated.

4.4.1 ECoG recording. ECoG data were recorded at 3052/1528 Hz (ECoG subject 1/ ECoG subject 2) from 118/96 electrodes through a 128-channel Tucker Davis Technologies recording system (<http://www.tdt.com>). Electrodes were localized on a postoperative computer tomography (CT) scan that was co-registered with a pre-operative MRI, and locations were corrected for the brain shift [6]. Electrodes that showed large artifacts or epileptic activity (as determined by the patient's neurologist) were excluded from analysis (7/35 electrodes were

excluded in subject 1/subject 2). Off-line, data were re-referenced to the common average, low-pass filtered and resampled at 1000Hz for computational purposes using the Matlab resample function. Line noise was removed at 60, 120 and 180 Hz using a 3rd order Butterworth filter.

4.4.2 ECoG analyses. Broadband and narrowband gamma responses were quantified as before [38]. We calculated power spectra and separated ECoG responses into broadband and narrowband gamma band spectral power increases. To control for the influence of evoked activity on the spectrum, event related potentials (ERPs) were calculated per condition and the condition specific ERP was regressed from each trial. This procedure makes sure that the broadband increase is not due to a sharp edge in the ERP; the same pattern of results is obtained if this step is omitted. For each condition, the average power spectral density was calculated every 1 Hz by Welch's method [104] from 0–500 ms after stimulus onset (and 0–500 ms after stimulus offset for the baseline) and a 250 ms Hann window to attenuate edge effects. ECoG power spectra are known to obey a power law and to capture broadband and narrowband gamma increases separately the following function was fitted to the average log spectrum from 35 to 200Hz (leaving out 60Hz line noise and harmonics) from each condition (Fig 3):

$$P(x) = (\beta_{broadband} - nx) + \beta_{narrowband} G(x|\mu, \sigma)$$

In which,

$$x = \log_{10}(\text{frequency})$$

$$G(x|\mu, \sigma) = e^{-\frac{(x-\mu)^2}{2\sigma^2}}$$

with $10^\sigma = 1.1$ Hz and $35 \text{ Hz} < 10^\mu < 80 \text{ Hz}$.

The slope of the log-log spectral power function (n) was fixed for each electrode by fitting it based on the average power spectrum of the baseline. For cross-validation, trials were split into even and odd repeats, and broadband and gamma changes were calculated for each. Confidence intervals were calculated by a bootstrap procedure. For each condition C with N_c trials, N_c trials were drawn randomly with replacement and power spectra were averaged. The parameters β were fitted on the average log power spectrum from these bootstrapped trials. This was repeated 100 times, resulting in two sets of distributions of broadband and gamma weights for even and odd trials.

Alpha response amplitude was calculated as follows. Alpha changes are best visible after the initial onset transient and ERP, and we used the power from 250–500 ms to calculate the alpha decreases for each stimulus. Alpha amplitude was calculated by averaging the log-power between 8 and 13 Hz.

4.4.3 Electrode selection. Electrodes for analysis were selected on the basis of three criteria. First, the pRF was located within V1, V2, and V3. Second, the explained variance in a pRF experiment was >15% [11]. Third, the center of the pRF was within the extent of the stimulus (<12 deg) and on the contralateral visual field. Because ECoG subject 2 did not have pRF data, only anatomical estimates of V1, V2, and V3 were used [105]. These criteria yielded 22 electrodes (19 from ECoG S1, 3 from ECoG S2).

4.5 fMRI procedure

fMRI data was measured from four subjects (three female, ages 22–42) with normal or corrected-to-normal vision at the Center for Brain Imaging at NYU. Informed, written consent was obtained from all subjects. The fMRI protocols were approved by the New York University

IRB. fMRI data were preprocessed and analyzed using custom software (<http://vistalab.stanford.edu/software>). Disc regions of interest (ROIs) (radius = 2 mm) were defined in fMRI subjects to match the position of the electrodes in ECoG subjects using a combination of anatomy, pRF centers, and visual field maps. The similarity between the ROI position and electrode position was compared via visual inspection of anatomical images and pRF centers (S3 Fig).

4.5.1 fMRI recording. Anatomical MRI and fMRI data were collected at the Center for Brain Imaging at NYU on a Siemens Allegra 3T head-only scanner with a Nova Medical transmit/receive coil (NMG11) and a Nova Medical phased array, 8-channel receive surface coil (NMSC072).

Two to three T1-weighted whole-brain anatomical scans (MPRAGE sequence) were obtained for each subject (voxel size: 1x1x1 mm, TR: 2500 ms; TE: 3.93 ms, flip angle: 8 deg). Functional images were collected using gradient echo, echo-planar imaging (voxel size: 2x2x2 mm, 24 slices, TR: 1500 ms, TE: 30 ms, flip angle: 72 deg). Images were corrected for B0 field inhomogeneity during offline image reconstruction using a separate field map measurement made halfway through the scan session. Slice prescription was set approximately perpendicular to the calcarine sulcus, covering the occipital lobe. In addition, a T1-weighted inplane was collected with the same slice prescription to align functional images to the high-resolution anatomical images.

4.5.2 fMRI analysis. Preprocessing. Anatomical images were coregistered and segmented into gray/white matter voxels using FreeSurfer autosegmentation algorithm (surfer.nmr.mgh.harvard.edu). A 3D mesh of the cortical surface was inflated for ease of visualization. Functional data were preprocessed and analyzed using custom software (<http://vistalab.stanford.edu/software>). Data were slice-time corrected to adjust for differences in acquisition time among slices in the 1.5-second frame. Data were motion corrected for both between- and within-scan motion. Finally, data were high-pass filtered for low-frequency drift [106] by multiple moving average smoothing (2 iterations, 40 seconds). Data were then converted to percent signal change by dividing each voxel's signal by its mean signal. The first 4 frames of each run (6 seconds) were discarded to allow longitudinal magnetization and the hemodynamic response to reach steady state.

Analysis. Noise was removed from the fMRI data using GLMdenoise, a variant of the standard GLM commonly used in fMRI analysis [107]. In brief, GLMdenoise derives noise regressors for each subject by performing principle components analysis on noise voxels that are unrelated to the task. The optimal number of noise regressors is selected based on improvement in cross-validated R^2 . The final model is fitted to each voxel's time series and bootstrapped 100 times over 8 runs. Here, the predictors in the GLM were the 9 image categories (4 gratings, 4 noise patterns, 1 plaid) and a blank period (a randomly assigned blank block). Voxel bootstraps were averaged across voxels within a ROI. The resulting 100 bootstraps per ROI were vector-length normalized and averaged across subjects. The beta estimate for each condition is taken as the median averaged bootstrap and the standard error as one-half the 68% confidence interval.

pRF model. The pRF runs were analyzed by fitting a 2D Gaussian to each voxel, modeling its pRF [108]. The pRF is defined by center location (x, y coordinates) and spread (σ). The resulting maps were used to define retinotopic areas V1, V2, and V3 as in [109].

4.6 Predicting fMRI signals directly from ECoG models

The relationship between fMRI and ECoG signals was analyzed using a linear regression model. The cross-validated coefficient of determination (R^2) was used as a metric for model

accuracy, and the regression coefficients were used to test whether ECoG predictors (broadband, gamma, and alpha) had a positive or negative relation with BOLD.

The relationship between fMRI and ECoG signals was analyzed using a linear regression model:

$$y = Xb + c + \varepsilon$$

where y is a vector of fMRI amplitudes (beta estimates), with n entries for the n different stimuli; X is a matrix of ECoG responses, n by 1, 2, or 3, where the columns correspond to one or more of broadband, gamma, and alpha estimates; b are the 1, 2, or 3 beta weights for the broadband, gamma, and alpha estimates; c is a constant (the y -intercept); and ε is the residual error term. The model was fitted separately for each cortical site (electrode/ROI pair) and for different combinations of predictors—broadband alone, gamma alone, alpha alone, each pairwise combination, and all three predictors together.

The n stimuli in the regressions included the contrast patterns and the blank stimulus. Inclusion of the blank stimulus is important for capturing the sign of the mean response. For example, if all contrast patterns induced a BOLD response of a particular level (say, +1) and induced ECoG responses of a particular level (say, -1) and we did not include the blank stimulus in the regression, then after subtracting the mean from each measure, all beta estimates would be approximately 0. This would mask a systematic relationship between ECoG and BOLD measures (in this example, an anticorrelation) arising from viewing stimuli with contrast compared to viewing a blank screen.

Models were evaluated by split-half cross-validation. First, the regression model $y_i = X_i b_i + c_i + \varepsilon$ was fit using half of the fMRI subjects (1 and 2) and half of the ECoG stimulus repetitions (even repetitions). To cross-validate this model, the beta values (b_i) were then applied to the left out half of the ECoG data (odd stimulus repetitions) to predict the left out half of the fMRI data (fMRI subjects 3 and 4). The same procedure was applied by reversing the training and testing data. This resulted in two testing datasets with BOLD responses predicted from ECoG for each stimulus condition ($X_i b_i + c_i$) and an actual measured BOLD value. For each cortical site, the coefficient of determination (see below) was calculated between the concatenated predictions and BOLD data values of the two test sets. All R^2 values reported in the results are cross-validated in this manner. The same pattern of results was achieved if instead of cross-validation, we solved the models on the complete datasets and computed the R^2 adjusted for the number of regressors.

To test whether different ECoG predictors (broadband, narrowband, alpha) had a positive or negative relation with BOLD, we tested whether the regression coefficient was significantly larger or smaller than 0. The regression coefficient was considered to be significantly different from 0 using a bootstrap statistic: for each model, the median of the beta values across sites was calculated after resampling 10,000 times. If <2.5% of the resampled statistics were smaller than zero, the beta values were considered significantly positive, and similarly, if <2.5% of the resampled statistics were greater than 0, the beta values were considered significantly negative.

4.7 Model accuracy

All model predictions were quantified using the coefficient of determination on cross-validated predictions. For predicting BOLD data from simulations of population neuronal activity (Fig 7, S7 Fig), the predicted BOLD has arbitrary units. In these cases, the observed BOLD and the predicted BOLD were both normalized by subtracting the mean and then dividing by the vector length. When predicting BOLD responses from features of the LFP data (broadband,

gamma, and alpha) by regression, the predicted BOLD data were in the same units as the measured BOLD, and no normalizing or rescaling was done.

To quantify the accuracy of the models, we calculated the cross-validated coefficient of determination, R^2 :

$$R^2 = 1 - \frac{SS_{residuals}}{SS_{data}}$$

$$SS_{residuals} = \sum_i (y_i - f_i)^2$$

$$SS_{data} = \sum_i (y_i - \bar{y})^2$$

where y are the data values and f are the prediction values. Because the model fits are cross-validated, it is possible for the model errors (residuals) to be larger than the data values, hence R^2 can be lower than 0, and spans $(-\infty, 1]$. In the case in which the model predictions and the data are unrelated and each are normally distributed with equal variance, R^2 will tend to -1 .

Supporting information

S1 Fig. Alpha changes explain additional variance in the blood-oxygen-level dependent (BOLD) response. **A)** Time/frequency spectrograms for the pink noise pattern and the grating in an exemplary V2 electrode show that power in the low frequencies decreased more for the pink noise pattern (left) than for the grating (right). **B)** Top: the correlation between broadband and BOLD shows that the broadband response underpredicts the BOLD response for the noise patterns (blue dots). Red and pink dots represent the gratings. This pattern is visible in most V2/V3 electrodes (**S5 Fig**) Bottom: taking into account the alpha decreases in the regression model explains the variance in the BOLD response that was not explained by the broadband changes. The R^2 represents the cross-validated coefficient of determination. (TIF)

S2 Fig. Electrocorticographic (ECoG) and functional magnetic resonance imaging (fMRI) measurements. **A)** ECoG and fMRI responses were measured to 8 different stationary stimuli. In all experiments, subjects were instructed to fixate on a dot at the center of the screen that alternated between red and green, changing colors at random times. Subjects pressed a button when the fixation dot changed color. ECoG Subject 2 did not make manual responses because these responses were found to interfere with visual fixation. **B)** ECoG responses were measured in an event-related design, in which stimuli were presented every 1000 milliseconds. Stimuli were presented for 500 milliseconds followed by a blank screen. **C)** Stimuli were presented in blocks of 12 seconds during fMRI, followed by 12 seconds of blank. **D)** Example ECoG power spectrum for one electrode. ECoG data showed broadband increases (>100 Hz) compared to baseline, narrowband gamma increases around 40 HZ, and a decrease in alpha power around 10 Hz. **E)** The blood-oxygen-level dependent (BOLD) response increased in different levels for the different stimuli averaged across subjects. When averaging the BOLD signal across subjects, the percent signal change per subject was vector-length normalized, ($BOLD\ normalized_i = \frac{BOLD\ change_i}{NORM}$, for condition i , in which $NORM = \sqrt{\sum_i BOLD\ change_i^2}$). To then reestimate the percent signal change across subjects, the averaged vector-length-normalized values were multiplied by the average norm. (TIF)

S3 Fig. Region of interest (ROI) selection. **A)** Channels in electrocorticographic (ECoG) S1 selected for further analysis. These channels were located within V1 (red), V2 (blue), or V3 (green), had significant broadband or gamma response to any stimuli, and had population Receptive Fields (pRF) variance explained >0.15 . V1 sites 8 and 9 are indicated, since these had the largest gamma responses. **B)** Electrode ROIs in functional magnetic resonance imaging (fMRI) S1. Disc ROIs (radius = 2 mm) were defined to have similar anatomical and retinotopic position as the ECoG Channels. **C)** The pRF centers for fMRI ROIs (filled circles) were chosen to be close to those for ECoG electrodes (open circles). Because the pRF centers measured with fMRI do not completely cover the visual field map, the locations can differ slightly. (TIF)

S4 Fig. Broadband, gamma, and alpha changes in V1, V2, and V3. **(A)** For each electrocorticographic (ECoG) electrode, for each stimulus condition, the broadband change was calculated. The average \log_{10} power from the inter stimulus baseline period was subtracted. The mean change from the baseline was then averaged across the 8–10 stimuli. **(B and C)** The same as A) shown for gamma and alpha. **(D)** For each ECoG electrode, for each stimulus condition, the blood-oxygen-level dependent (BOLD) percent signal change was calculated. The mean change from the baseline was then averaged across the stimuli. (TIF)

S5 Fig. Correlation between blood-oxygen-level dependent (BOLD) and electrocorticographic (ECoG) broadband, gamma, and alpha for all electrodes. Correlation between BOLD and ECoG in V1 and V2/V3. The R^2 is cross-validated: beta values are calculated from half the ECoG trials and half the functional magnetic resonance imaging (fMRI) subjects, and the regression model is tested on the other half of the trials and subjects. (TIF)

S6 Fig. Blood-oxygen-level dependent (BOLD) predicted by electrocorticographic (ECoG) broadband and alpha for all electrodes. This plot shows the predicted BOLD (x -axis) versus measured BOLD (y -axis) for the 9 V1 sites (top) and 13 V2/V3 sites (bottom), based on a linear regression of the broadband and alpha components of the ECoG signals. The coefficient of determination, R^2 , was cross-validated. (TIF)

S7 Fig. Accuracy of blood-oxygen-level dependent (BOLD) predictions from simulated neuronal activity. This plot shows the predicted BOLD (x -axis) versus measured BOLD (y -axis) for the 9 V1 sites (top) and 13 V2/V3 sites (bottom). Each color corresponds to one site. The cross-validated coefficient of determination (R^2) was computed separately for each of the 9 sites and then averaged. The different subplots are models solved with different constraints. In the main text of the paper, model parameters were fit with three constraints: (1) the C^1 (broadband) time series had a fixed, nonzero level (but could vary in correlation between neurons), (2) the C^2 (gamma) time series had a fixed, nonzero level (but could vary in correlation), and (3) the C^3 time series had a fixed, nonzero correlation (but could vary in level). The model predictions based on these constraints are plotted in the upper left of both the upper panel (V1) and the lower panel (V2/V3). Seven alternative models were run, and their predictions are shown in the remaining panels. For these models, the three input types, C^1 , C^2 , and C^3 , were constrained to have time series varying in either the level or correlations across neurons but not both. (TIF)

S8 Fig. The size of the electrocorticographic (ECoG) response and how well ECoG and blood-oxygen-level dependent (BOLD) are correlated. Variance in the BOLD response

explained by ECoG (R^2 , the coefficient of determination) as a function of the size of the ECoG response. Each dot represents 1 electrode. *x*-axis: for each electrode, ECoG broadband, gamma, and alpha responses were averaged across (nonbaseline) stimuli. *y*-axis: the cross-validated R^2 when BOLD is explained by broadband (left), gamma (middle), and alpha (right). (TIF)

S9 Fig. Relation between the simulated and measured local field potential (LFP) values.

Every dot represents the broadband (black), gamma (magenta), or alpha (green) power change for one electrode, one stimulus condition. The power changes in the LFP are driven by changes in parameters C^1 , C^2 , and C^3 . We fitted these parameters such that the simulated LFP values for broadband, gamma, and alpha nicely match the measured values. (TIF)

Acknowledgments

We thank two colleagues for making important contributions to our analytic framework. David J Heeger (NYU) proposed to us that the two measures, BOLD and LFP, could be approximated by the same operations computed in a different order (captured in Eqs 1–3), and Weiji Ma (NYU) derived a variant of Eq 4 for us, expressing analytically the quantitative difference that results from the difference in the order of operations. We thank Josef Parvizi for his help in recording the ECoG data, and we thank Brian A. Wandell, David J. Heeger, Rachel Denison, Noah Benson, and Nathan Witthoft for helpful comments on an earlier draft of the manuscript.

Author Contributions

Conceptualization: Dora Hermes, Jonathan Winawer.

Data curation: Dora Hermes, Mai Nguyen, Jonathan Winawer.

Formal analysis: Dora Hermes, Mai Nguyen, Jonathan Winawer.

Funding acquisition: Dora Hermes, Jonathan Winawer.

Investigation: Dora Hermes, Mai Nguyen, Jonathan Winawer.

Methodology: Dora Hermes, Mai Nguyen, Jonathan Winawer.

Project administration: Dora Hermes, Mai Nguyen, Jonathan Winawer.

Resources: Dora Hermes, Jonathan Winawer.

Software: Dora Hermes, Mai Nguyen, Jonathan Winawer.

Supervision: Dora Hermes, Jonathan Winawer.

Validation: Dora Hermes, Jonathan Winawer.

Visualization: Dora Hermes, Mai Nguyen, Jonathan Winawer.

Writing – original draft: Dora Hermes, Jonathan Winawer.

Writing – review & editing: Dora Hermes, Jonathan Winawer.

References

1. Logothetis NK, Wandell BA. Interpreting the BOLD signal. *Annu Rev Physiol*. 2004; 66:735–69. Epub 2004/02/24. <https://doi.org/10.1146/annurev.physiol.66.082602.092845> PMID: 14977420.

2. Buzsaki G, Anastassiou CA, Koch C. The origin of extracellular fields and currents—EEG, ECoG, LFP and spikes. *Nature reviews Neuroscience*. 2012; 13(6):407–20. <https://doi.org/10.1038/nrn3241> PMID: 22595786.
3. Hämäläinen M, Hari R, Ilmoniemi RJ, Knuutila J, Lounasmaa OV. Magnetoencephalography—theory, instrumentation, and applications to noninvasive studies of the working human brain. *Reviews of modern Physics*. 1993; 65(2):413.
4. George JS, Aine CJ, Mosher JC, Schmidt DM, Ranken DM, Schlitt HA, et al. Mapping function in the human brain with magnetoencephalography, anatomical magnetic resonance imaging, and functional magnetic resonance imaging. *J Clin Neurophysiol*. 1995; 12(5):406–31. PMID: 8576388.
5. Cottareau BR, Ales JM, Norcia AM. How to use fMRI functional localizers to improve EEG/MEG source estimation. *Journal of neuroscience methods*. 2015; 250:64–73. <https://doi.org/10.1016/j.jneumeth.2014.07.015> PMID: 25088693; PubMed Central PMCID: PMCPCMC4383720.
6. Hermes D, Miller KJ, Noordmans HJ, Vansteensel MJ, Ramsey NF. Automated electrocorticographic electrode localization on individually rendered brain surfaces. *Journal of neuroscience methods*. 2010; 185(2):293–8. Epub 2009/10/20. <https://doi.org/10.1016/j.jneumeth.2009.10.005> PMID: 19836416.
7. Huk AC, Ress D, Heeger DJ. Neuronal basis of the motion aftereffect reconsidered. *Neuron*. 2001; 32(1):161–72. PMID: 11604147.
8. Ales JM, Norcia AM. Assessing direction-specific adaptation using the steady-state visual evoked potential: results from EEG source imaging. *J Vis*. 2009; 9(7):8. <https://doi.org/10.1167/9.7.8> PMID: 19761323.
9. Pestilli F, Carrasco M, Heeger DJ, Gardner JL. Attentional enhancement via selection and pooling of early sensory responses in human visual cortex. *Neuron*. 2011; 72(5):832–46. Epub 2011/12/14. <https://doi.org/10.1016/j.neuron.2011.09.025> PMID: 22153378; PubMed Central PMCID: PMC3264681.
10. Itthipuripat S, Ester EF, Deering S, Serences JT. Sensory gain outperforms efficient readout mechanisms in predicting attention-related improvements in behavior. *J Neurosci*. 2014; 34(40):13384–98. Epub 2014/10/03. <https://doi.org/10.1523/JNEUROSCI.2277-14.2014> PMID: 25274817; PubMed Central PMCID: PMC4180474.
11. Winawer J, Kay KN, Foster BL, Rauschecker AM, Parvizi J, Wandell BA. Asynchronous broadband signals are the principal source of the BOLD response in human visual cortex. *Curr Biol*. 2013; 23(13):1145–53. <https://doi.org/10.1016/j.cub.2013.05.001> PMID: 23770184; PubMed Central PMCID: PMCPCMC3710543.
12. Goense JB, Logothetis NK. Neurophysiology of the BOLD fMRI signal in awake monkeys. *Current biology: CB*. 2008; 18(9):631–40. Epub 2008/04/29. <https://doi.org/10.1016/j.cub.2008.03.054> PMID: 18439825.
13. Niessing J, Ebisch B, Schmidt KE, Niessing M, Singer W, Galuske RA. Hemodynamic signals correlate tightly with synchronized gamma oscillations. *Science*. 2005; 309(5736):948–51. Epub 2005/08/06. <https://doi.org/10.1126/science.1110948> PMID: 16081740.
14. Mukamel R, Gelbard H, Arieli A, Hasson U, Fried I, Malach R. Coupling between neuronal firing, field potentials, and FMRI in human auditory cortex. *Science*. 2005; 309(5736):951–4. <https://doi.org/10.1126/science.1110913> PMID: 16081741.
15. Shmuel A, Augath M, Oeltermann A, Logothetis NK. Negative functional MRI response correlates with decreases in neuronal activity in monkey visual area V1. *Nature neuroscience*. 2006; 9(4):569–77. Epub 2006/03/21. <https://doi.org/10.1038/nn1675> PMID: 16547508.
16. Logothetis NK, Pauls J, Augath M, Trinath T, Oeltermann A. Neurophysiological investigation of the basis of the fMRI signal. *Nature*. 2001; 412(6843):150–7. Epub 2001/07/13. <https://doi.org/10.1038/35084005> PMID: 11449264.
17. Lachaux JP, Fonlupt P, Kahane P, Minotti L, Hoffmann D, Bertrand O, et al. Relationship between task-related gamma oscillations and BOLD signal: new insights from combined fMRI and intracranial EEG. *Hum Brain Mapp*. 2007; 28(12):1368–75. <https://doi.org/10.1002/hbm.20352> PMID: 17274021.
18. Muthukumaraswamy SD, Singh KD. Functional decoupling of BOLD and gamma-band amplitudes in human primary visual cortex. *Hum Brain Mapp*. 2009; 30(7):2000–7. <https://doi.org/10.1002/hbm.20644> PMID: 18729078.
19. Swettenham JB, Muthukumaraswamy SD, Singh KD. BOLD Responses in Human Primary Visual Cortex are Insensitive to Substantial Changes in Neural Activity. *Front Hum Neurosci*. 2013; 7:76. Epub 2013/03/14. <https://doi.org/10.3389/fnhum.2013.00076> PMID: 23482840; PubMed Central PMCID: PMC3593627.
20. Maier A, Wilke M, Aura C, Zhu C, Ye FQ, Leopold DA. Divergence of fMRI and neural signals in V1 during perceptual suppression in the awake monkey. *Nature neuroscience*. 2008; 11(10):1193–200.

- Epub 2008/08/20. <https://doi.org/10.1038/nn.2173> PMID: 18711393; PubMed Central PMCID: PMC2754054.
21. Scheeringa R, Fries P, Petersson KM, Oostenveld R, Grothe I, Norris DG, et al. Neuronal dynamics underlying high- and low-frequency EEG oscillations contribute independently to the human BOLD signal. *Neuron*. 2011; 69(3):572–83. Epub 2011/02/15. <https://doi.org/10.1016/j.neuron.2010.11.044> PMID: 21315266.
 22. Harvey BM, Vansteensel MJ, Ferrier CH, Petridou N, Zuiderbaan W, Aarnoutse EJ, et al. Frequency specific spatial interactions in human electrocorticography: V1 alpha oscillations reflect surround suppression. *Neuroimage*. 2013; 65:424–32. Epub 2012/10/23. <https://doi.org/10.1016/j.neuroimage.2012.10.020> PMID: 23085107.
 23. Scheeringa R, Koopmans PJ, van Mourik T, Jensen O, Norris DG. The relationship between oscillatory EEG activity and the laminar-specific BOLD signal. *Proc Natl Acad Sci U S A*. 2016. Epub 2016/06/02. <https://doi.org/10.1073/pnas.1522577113> PMID: 27247416.
 24. Lima B, Cardoso MM, Sirotin YB, Das A. Stimulus-related neuroimaging in task-engaged subjects is best predicted by concurrent spiking. *J Neurosci*. 2014; 34(42):13878–91. Epub 2014/10/17. <https://doi.org/10.1523/JNEUROSCI.1595-14.2014> PMID: 25319685; PubMed Central PMCID: PMC4198534.
 25. Rees G, Friston K, Koch C. A direct quantitative relationship between the functional properties of human and macaque V5. *Nat Neurosci*. 2000; 3(7):716–23. <https://doi.org/10.1038/76673> PMID: 10862705.
 26. Heeger DJ, Huk AC, Geisler WS, Albrecht DG. Spikes versus BOLD: what does neuroimaging tell us about neuronal activity? *Nat Neurosci*. 2000; 3(7):631–3. <https://doi.org/10.1038/76572> PMID: 10862687.
 27. Heeger DJ, Ress D. What does fMRI tell us about neuronal activity? *Nature reviews Neuroscience*. 2002; 3(2):142–51. <https://doi.org/10.1038/nrn730> PMID: 11836522.
 28. Mathiesen C, Caesar K, Akgoren N, Lauritzen M. Modification of activity-dependent increases of cerebral blood flow by excitatory synaptic activity and spikes in rat cerebellar cortex. *J Physiol*. 1998; 512 (Pt 2):555–66. <https://doi.org/10.1111/j.1469-7793.1998.555be.x> PMID: 9763643; PubMed Central PMCID: PMCPMC2231204.
 29. Lee JH, Durand R, Gradinaru V, Zhang F, Goshen I, Kim DS, et al. Global and local fMRI signals driven by neurons defined optogenetically by type and wiring. *Nature*. 2010; 465(7299):788–92. <https://doi.org/10.1038/nature09108> PMID: 20473285; PubMed Central PMCID: PMCPMC3177305.
 30. Zanos TP, Mineault PJ, Pack CC. Removal of spurious correlations between spikes and local field potentials. *Journal of neurophysiology*. 2011; 105(1):474–86. <https://doi.org/10.1152/jn.00642.2010> PMID: 21068271.
 31. Pesaran B. Spectral analysis for neural signals. In: Mitra P, editor. *Neural Signal Processing: Quantitative Analysis of Neural Activity*. Society for Neuroscience; 2008. p. 1–12.
 32. Raichle ME, Mintun MA. Brain work and brain imaging. *Annu Rev Neurosci*. 2006; 29:449–76. <https://doi.org/10.1146/annurev.neuro.29.051605.112819> PMID: 16776593.
 33. Attwell D, Buchan AM, Charkpak S, Lauritzen M, Macvicar BA, Newman EA. Glial and neuronal control of brain blood flow. *Nature*. 2010; 468(7321):232–43. <https://doi.org/10.1038/nature09613> PMID: 21068832; PubMed Central PMCID: PMCPMC3206737.
 34. Caesar K, Gold L, Lauritzen M. Context sensitivity of activity-dependent increases in cerebral blood flow. *Proc Natl Acad Sci U S A*. 2003; 100(7):4239–44. <https://doi.org/10.1073/pnas.0635075100> PMID: 12655065; PubMed Central PMCID: PMCPMC153077.
 35. Uhlirova H, Kilic K, Tian P, Thunemann M, Desjardins M, Saisan PA, et al. Cell type specificity of neurovascular coupling in cerebral cortex. *Elife*. 2016; 5. <https://doi.org/10.7554/eLife.14315> PMID: 27244241; PubMed Central PMCID: PMCPMC4933561.
 36. Yu BM, Cunningham JP, Santhanam G, Ryu SI, Shenoy KV, Sahani M. Gaussian-process factor analysis for low-dimensional single-trial analysis of neural population activity. *Journal of neurophysiology*. 2009; 102(1):614–35. <https://doi.org/10.1152/jn.90941.2008> PMID: 19357332; PubMed Central PMCID: PMCPMC2712272.
 37. Stevenson IH, Kording KP. How advances in neural recording affect data analysis. *Nat Neurosci*. 2011; 14(2):139–42. <https://doi.org/10.1038/nn.2731> PMID: 21270781; PubMed Central PMCID: PMCPMC3410539.
 38. Hermes D, Miller KJ, Wandell BA, Winawer J. Stimulus dependence of gamma oscillations in human visual cortex. *Cerebral cortex*. 2015; 25(9):2951–9. Epub 2014/05/24. <https://doi.org/10.1093/cercor/bhu091> PMID: 24855114; PubMed Central PMCID: PMC4537439.

39. Koch C, Rapp M, Segev I. A brief history of time (constants). *Cereb Cortex*. 1996; 6(2):93–101. PMID: [8670642](#).
40. Miller KJ, Sorensen LB, Ojemann JG, den Nijs M. Power-law scaling in the brain surface electric potential. *PLoS Comput Biol*. 2009; 5(12):e1000609. Epub 2009/12/19. <https://doi.org/10.1371/journal.pcbi.1000609> PMID: [20019800](#); PubMed Central PMCID: [PMC2787015](#).
41. Henrie JA, Shapley R. LFP power spectra in V1 cortex: the graded effect of stimulus contrast. *Journal of neurophysiology*. 2005; 94(1):479–90. <https://doi.org/10.1152/jn.00919.2004> PMID: [15703230](#).
42. Tan AY, Chen Y, Scholl B, Seidemann E, Priebe NJ. Sensory stimulation shifts visual cortex from synchronous to asynchronous states. *Nature*. 2014; 509(7499):226–9. <https://doi.org/10.1038/nature13159> PMID: [24695217](#); PubMed Central PMCID: [PMCPMC4067243](#).
43. Jia X, Tanabe S, Kohn A. gamma and the coordination of spiking activity in early visual cortex. *Neuron*. 2013; 77(4):762–74. <https://doi.org/10.1016/j.neuron.2012.12.036> PMID: [23439127](#); PubMed Central PMCID: [PMCPMC3632874](#).
44. Hasenstaub A, Shu Y, Haider B, Kraushaar U, Duque A, McCormick DA. Inhibitory postsynaptic potentials carry synchronized frequency information in active cortical networks. *Neuron*. 2005; 47(3):423–35. <https://doi.org/10.1016/j.neuron.2005.06.016> PMID: [16055065](#).
45. Gray CM, Konig P, Engel AK, Singer W. Oscillatory responses in cat visual cortex exhibit inter-columnar synchronization which reflects global stimulus properties. *Nature*. 1989; 338(6213):334–7. Epub 1989/03/23. <https://doi.org/10.1038/338334a0> PMID: [2922061](#).
46. Gray CM, Singer W. Stimulus-specific neuronal oscillations in orientation columns of cat visual cortex. *Proceedings of the National Academy of Sciences of the United States of America*. 1989; 86(5):1698–702. Epub 1989/03/01. PMID: [2922407](#); PubMed Central PMCID: [PMC286768](#).
47. Perrenoud Q, Pennartz CM, Gentet LJ. Membrane Potential Dynamics of Spontaneous and Visually Evoked Gamma Activity in V1 of Awake Mice. *PLoS Biol*. 2016; 14(2):e1002383. Epub 2016/02/20. <https://doi.org/10.1371/journal.pbio.1002383> PMID: [26890123](#).
48. Burns SP, Xing D, Shapley RM. Is gamma-band activity in the local field potential of V1 cortex a "clock" or filtered noise? *J Neurosci*. 2011; 31(26):9658–64. Epub 2011/07/01. <https://doi.org/10.1523/JNEUROSCI.0660-11.2011> PMID: [21715631](#); PubMed Central PMCID: [PMC3518456](#).
49. Jensen O, Mazaheri A. Shaping functional architecture by oscillatory alpha activity: gating by inhibition. *Front Hum Neurosci*. 2010; 4:186. <https://doi.org/10.3389/fnhum.2010.00186> PMID: [21119777](#); PubMed Central PMCID: [PMCPMC2990626](#).
50. Schalk G. A general framework for dynamic cortical function: the function-through-biased-oscillations (FBO) hypothesis. *Front Hum Neurosci*. 2015; 9:352. Epub 2015/07/03. <https://doi.org/10.3389/fnhum.2015.00352> PMID: [26136676](#); PubMed Central PMCID: [PMC4468375](#).
51. Llinas RR, Grace AA, Yarom Y. In vitro neurons in mammalian cortical layer 4 exhibit intrinsic oscillatory activity in the 10- to 50-Hz frequency range. *Proc Natl Acad Sci U S A*. 1991; 88(3):897–901. PMID: [1992481](#); PubMed Central PMCID: [PMCPMC50921](#).
52. Ojemann GA, Ojemann J, Ramsey NF. Relation between functional magnetic resonance imaging (fMRI) and single neuron, local field potential (LFP) and electrocorticography (ECoG) activity in human cortex. *Front Hum Neurosci*. 2013; 7:34. Epub 2013/02/23. <https://doi.org/10.3389/fnhum.2013.00034> PMID: [23431088](#); PubMed Central PMCID: [PMC3576621](#).
53. Hermes D, Miller KJ, Wandell BA, Winawer J. Gamma oscillations in visual cortex: the stimulus matters. *Trends Cogn Sci*. 2015; 19(2):57–8. <https://doi.org/10.1016/j.tics.2014.12.009> PMID: [25575448](#); PubMed Central PMCID: [PMCPMC4395850](#).
54. Ray S, Maunsell JH. Different origins of gamma rhythm and high-gamma activity in macaque visual cortex. *PLoS Biol*. 2011; 9(4):e1000610. Epub 2011/05/03. <https://doi.org/10.1371/journal.pbio.1000610> PMID: [21532743](#); PubMed Central PMCID: [PMC3075230](#).
55. Singer W. Neuronal synchrony: a versatile code for the definition of relations? *Neuron*. 1999; 24(1):49–65, 111–25. PMID: [10677026](#).
56. Buzsaki G, Wang XJ. Mechanisms of gamma oscillations. *Annu Rev Neurosci*. 2012; 35:203–25. <https://doi.org/10.1146/annurev-neuro-062111-150444> PMID: [22443509](#); PubMed Central PMCID: [PMC4049541](#).
57. Miller KJ, Zanos S, Fetz EE, den Nijs M, Ojemann JG. Decoupling the cortical power spectrum reveals real-time representation of individual finger movements in humans. *J Neurosci*. 2009; 29(10):3132–7. Epub 2009/03/13. <https://doi.org/10.1523/JNEUROSCI.5506-08.2009> PMID: [19279250](#).
58. Manning JR, Jacobs J, Fried I, Kahana MJ. Broadband shifts in local field potential power spectra are correlated with single-neuron spiking in humans. *J Neurosci*. 2009; 29(43):13613–20. Epub 2009/10/30. <https://doi.org/10.1523/JNEUROSCI.2041-09.2009> PMID: [19864573](#); PubMed Central PMCID: [PMC3001247](#).

59. Musall S, von Pfohl V, Rauch A, Logothetis NK, Whittingstall K. Effects of neural synchrony on surface EEG. *Cereb Cortex*. 2014; 24(4):1045–53. <https://doi.org/10.1093/cercor/bhs389> PMID: 23236202.
60. Engell AD, Huettel S, McCarthy G. The fMRI BOLD signal tracks electrophysiological spectral perturbations, not event-related potentials. *Neuroimage*. 2012; 59(3):2600–6. <https://doi.org/10.1016/j.neuroimage.2011.08.079> PMID: 21925278; PubMed Central PMCID: PMC3277784.
61. Sirotin YB, Das A. Anticipatory haemodynamic signals in sensory cortex not predicted by local neuronal activity. *Nature*. 2009; 457(7228):475–9. Epub 2009/01/23. <https://doi.org/10.1038/nature07664> PMID: 19158795; PubMed Central PMCID: PMC2705195.
62. Burns SP, Xing D, Shapley RM. Comparisons of the dynamics of local field potential and multiunit activity signals in macaque visual cortex. *J Neurosci*. 2010; 30(41):13739–49. Epub 2010/10/15. <https://doi.org/10.1523/JNEUROSCI.0743-10.2010> PMID: 20943914; PubMed Central PMCID: PMC3518461.
63. Jia X, Xing D, Kohn A. No consistent relationship between gamma power and peak frequency in macaque primary visual cortex. *J Neurosci*. 2013; 33(1):17–25. Epub 2013/01/04. <https://doi.org/10.1523/JNEUROSCI.1687-12.2013> PMID: 23283318; PubMed Central PMCID: PMC3560843.
64. Dalal SS, Baillet S, Adam C, Ducors A, Schwartz D, Jerbi K, et al. Simultaneous MEG and intracranial EEG recordings during attentive reading. *Neuroimage*. 2009; 45(4):1289–304. <https://doi.org/10.1016/j.neuroimage.2009.01.017> PMID: 19349241.
65. Adrian ED, Matthews BHC. The Berger rhythm: Potential changes from the occipital lobes in man. *Brain*. 1934; 57(4):355–85.
66. Norcia AM, Appelbaum LG, Ales JM, Cottareau BR, Rossion B. The steady-state visual evoked potential in vision research: A review. *J Vis*. 2015; 15(6):4. <https://doi.org/10.1167/15.6.4> PMID: 26024451; PubMed Central PMCID: PMC351566.
67. Winawer J, Parvizi J. Linking Electrical Stimulation of Human Primary Visual Cortex, Size of Affected Cortical Area, Neuronal Responses, and Subjective Experience. *Neuron*. 2016; 92(6):1213–9. <https://doi.org/10.1016/j.neuron.2016.11.008> PMID: 27939584; PubMed Central PMCID: PMC35182175.
68. Tallon-Baudry C, Bertrand O. Oscillatory gamma activity in humans and its role in object representation. *Trends Cogn Sci*. 1999; 3(4):151–62. PMID: 10322469.
69. Hermes D, Miller KJ, Vansteensel MJ, Aarnoutse EJ, Leijten FS, Ramsey NF. Neurophysiologic correlates of fMRI in human motor cortex. *Human brain mapping*. 2012; 33(7):1689–99. Epub 2011/06/22. <https://doi.org/10.1002/hbm.21314> PMID: 21692146.
70. Hermes D, Miller KJ, Vansteensel MJ, Edwards E, Ferrier CH, Bleichner MG, et al. Cortical theta wanes for language. *Neuroimage*. 2014; 85 Pt 2:738–48. Epub 2013/07/31. <https://doi.org/10.1016/j.neuroimage.2013.07.029> PMID: 23891904.
71. Magri C, Schridde U, Murayama Y, Panzeri S, Logothetis NK. The amplitude and timing of the BOLD signal reflects the relationship between local field potential power at different frequencies. *J Neurosci*. 2012; 32(4):1395–407. Epub 2012/01/27. <https://doi.org/10.1523/JNEUROSCI.3985-11.2012> PMID: 22279224.
72. Harris KD, Thiele A. Cortical state and attention. *Nature reviews Neuroscience*. 2011; 12(9):509–23. <https://doi.org/10.1038/nrn3084> PMID: 21829219; PubMed Central PMCID: PMC3324821.
73. Mazaheri A, Jensen O. Rhythmic pulsing: linking ongoing brain activity with evoked responses. *Front Hum Neurosci*. 2010; 4:177. <https://doi.org/10.3389/fnhum.2010.00177> PMID: 21060804; PubMed Central PMCID: PMC32972683.
74. Mazaheri A, Jensen O. Asymmetric amplitude modulations of brain oscillations generate slow evoked responses. *J Neurosci*. 2008; 28(31):7781–7. <https://doi.org/10.1523/JNEUROSCI.1631-08.2008> PMID: 18667610.
75. Raichle ME. Two views of brain function. *Trends in cognitive sciences*. 2010; 14(4):180–90. Epub 2010/03/09. <https://doi.org/10.1016/j.tics.2010.01.008> PMID: 20206576.
76. Samaha J, Gosseries O, Postle BR. Distinct Oscillatory Frequencies Underlie Excitability of Human Occipital and Parietal Cortex. *J Neurosci*. 2017; 37(11):2824–33. <https://doi.org/10.1523/JNEUROSCI.3413-16.2017> PMID: 28179556; PubMed Central PMCID: PMC5354329.
77. Dugue L, Marque P, VanRullen R. The phase of ongoing oscillations mediates the causal relation between brain excitation and visual perception. *J Neurosci*. 2011; 31(33):11889–93. <https://doi.org/10.1523/JNEUROSCI.1161-11.2011> PMID: 21849549.
78. Scheeringa R, Mazaheri A, Bojak I, Norris DG, Kleinschmidt A. Modulation of visually evoked cortical fMRI responses by phase of ongoing occipital alpha oscillations. *J Neurosci*. 2011; 31(10):3813–20. <https://doi.org/10.1523/JNEUROSCI.4697-10.2011> PMID: 21389236.

79. Kang K, Shelley M, Henrie JA, Shapley R. LFP spectral peaks in V1 cortex: network resonance and cortico-cortical feedback. *J Comput Neurosci*. 2010; 29(3):495–507. Epub 2009/10/29. <https://doi.org/10.1007/s10827-009-0190-2> PMID: 19862612; PubMed Central PMCID: PMC3050555.
80. Xing D, Shen Y, Burns S, Yeh CI, Shapley R, Li W. Stochastic generation of gamma-band activity in primary visual cortex of awake and anesthetized monkeys. *J Neurosci*. 2012; 32(40):13873–80a. <https://doi.org/10.1523/JNEUROSCI.5644-11.2012> PMID: 23035096; PubMed Central PMCID: PMC3752128.
81. Sloan HL, Austin VC, Blamire AM, Schnupp JW, Lowe AS, Allers KA, et al. Regional differences in neurovascular coupling in rat brain as determined by fMRI and electrophysiology. *Neuroimage*. 2010; 53(2):399–411. <https://doi.org/10.1016/j.neuroimage.2010.07.014> PMID: 20633665.
82. Conner CR, Ellmore TM, Pieters TA, DiSano MA, Tandon N. Variability of the relationship between electrophysiology and BOLD-fMRI across cortical regions in humans. *J Neurosci*. 2011; 31(36):12855–65. Epub 2011/09/09. <https://doi.org/10.1523/JNEUROSCI.1457-11.2011> PMID: 21900564; PubMed Central PMCID: PMC3322193.
83. Huo BX, Smith JB, Drew PJ. Neurovascular coupling and decoupling in the cortex during voluntary locomotion. *J Neurosci*. 2014; 34(33):10975–81. Epub 2014/08/15. <https://doi.org/10.1523/JNEUROSCI.1369-14.2014> PMID: 25122897; PubMed Central PMCID: PMC4131012.
84. Goense J, Merkle H, Logothetis NK. High-resolution fMRI reveals laminar differences in neurovascular coupling between positive and negative BOLD responses. *Neuron*. 2012; 76(3):629–39. <https://doi.org/10.1016/j.neuron.2012.09.019> PMID: 23141073.
85. Zaldivar D, Rauch A, Whittingstall K, Logothetis NK, Goense J. Dopamine-induced dissociation of BOLD and neural activity in macaque visual cortex. *Curr Biol*. 2014; 24(23):2805–11. <https://doi.org/10.1016/j.cub.2014.10.006> PMID: 25456449.
86. Attwell D, Laughlin SB. An energy budget for signaling in the grey matter of the brain. *J Cereb Blood Flow Metab*. 2001; 21(10):1133–45. <https://doi.org/10.1097/00004647-200110000-00001> PMID: 11598490.
87. Sokoloff L. Energetics of functional activation in neural tissues. *Neurochemical Research*. 1999; 24(2):321–9. PMID: 9972882
88. Uhlirva H, Kilic K, Tian P, Sakadzic S, Gagnon L, Thunemann M, et al. The roadmap for estimation of cell-type-specific neuronal activity from non-invasive measurements. *Philos Trans R Soc Lond B Biol Sci*. 2016; 371(1705). <https://doi.org/10.1098/rstb.2015.0356> PMID: 27574309; PubMed Central PMCID: PMC5003857.
89. Buxton RB, Uludag K, Dubowitz DJ, Liu TT. Modeling the hemodynamic response to brain activation. *Neuroimage*. 2004; 23 Suppl 1:S220–33. Epub 2004/10/27. <https://doi.org/10.1016/j.neuroimage.2004.07.013> PMID: 15501093.
90. Heeger DJ, Simoncelli EP, Movshon JA. Computational models of cortical visual processing. *Proc Natl Acad Sci U S A*. 1996; 93(2):623–7. PMID: 8570605; PubMed Central PMCID: PMC40101.
91. Carandini M, Heeger DJ. Normalization as a canonical neural computation. *Nature reviews Neuroscience*. 2012; 13(1):51–62. <https://doi.org/10.1038/nrn3136> PMID: 22108672; PubMed Central PMCID: PMC3273486.
92. Kay KN, Winawer J, Rokem A, Mezer A, Wandell BA. A two-stage cascade model of BOLD responses in human visual cortex. *PLoS Comput Biol*. 2013; 9(5):e1003079. Epub 2013/06/06. <https://doi.org/10.1371/journal.pcbi.1003079> PMID: 23737741; PubMed Central PMCID: PMC3667759.
93. Wandell BA. *Foundations of vision*. Sunderland, Mass.: Sinauer Associates; 1995. xvi, 476 p., [4] p. of plates p.
94. Carandini M, Demb JB, Mante V, Tolhurst DJ, Dan Y, Olshausen BA, et al. Do we know what the early visual system does? *J Neurosci*. 2005; 25(46):10577–97. <https://doi.org/10.1523/JNEUROSCI.3726-05.2005> PMID: 16291931.
95. Olshausen BA, Field DJ. How close are we to understanding v1? *Neural Comput*. 2005; 17(8):1665–99. <https://doi.org/10.1162/0899766054026639> PMID: 15969914.
96. Gavish M, Donoho D. Three Dream Applications of Verifiable Computational Results. *Computing in Science & Engineering*. 2012; 14(4):26–31.
97. LeVeque RJ, Mitchell IM, Stodden V. *Reproducible Research for Scientific Computing: Tools and Strategies for Changing the Culture*. Computing in Science & Engineering. 2012; 14(4):13–7.
98. Axelrod V. Minimizing bugs in cognitive neuroscience programming. *Frontiers in psychology*. 2014; 5. <https://doi.org/10.3389/fpsyg.2014.01435> PMID: 25566120
99. Bedard C, Destexhe A. Macroscopic models of local field potentials and the apparent 1/f noise in brain activity. *Biophys J*. 2009; 96(7):2589–603. <https://doi.org/10.1016/j.bpj.2008.12.3951> PMID: 19348744; PubMed Central PMCID: PMCPMC2711281.

100. Milstein J, Mormann F, Fried I, Koch C. Neuronal shot noise and Brownian 1/f² behavior in the local field potential. *PloS one*. 2009; 4(2):e4338. Epub 2009/02/05. <https://doi.org/10.1371/journal.pone.0004338> PMID: [19190760](https://pubmed.ncbi.nlm.nih.gov/19190760/); PubMed Central PMCID: PMC2629847.
101. Bedard C, Kroger H, Destexhe A. Does the 1/f frequency scaling of brain signals reflect self-organized critical states? *Phys Rev Lett*. 2006; 97(11):118102. <https://doi.org/10.1103/PhysRevLett.97.118102> PMID: [17025932](https://pubmed.ncbi.nlm.nih.gov/17025932/).
102. Logothetis NK, Kayser C, Oeltermann A. In vivo measurement of cortical impedance spectrum in monkeys: implications for signal propagation. *Neuron*. 2007; 55(5):809–23. <https://doi.org/10.1016/j.neuron.2007.07.027> PMID: [17785187](https://pubmed.ncbi.nlm.nih.gov/17785187/).
103. Jia X, Smith MA, Kohn A. Stimulus selectivity and spatial coherence of gamma components of the local field potential. *J Neurosci*. 2011; 31(25):9390–403. Epub 2011/06/24. <https://doi.org/10.1523/JNEUROSCI.0645-11.2011> PMID: [21697389](https://pubmed.ncbi.nlm.nih.gov/21697389/); PubMed Central PMCID: PMC3133446.
104. Welch PD. Use of Fast Fourier Transform for Estimation of Power Spectra—a Method Based on Time Averaging over Short Modified Periodograms. *Ieee T Acoust Speech*. 1967; Au 15(2):70–&.
105. Benson NC, Butt OH, Datta R, Radoeva PD, Brainard DH, Aguirre GK. The retinotopic organization of striate cortex is well predicted by surface topology. *Curr Biol*. 2012; 22(21):2081–5. <https://doi.org/10.1016/j.cub.2012.09.014> PMID: [23041195](https://pubmed.ncbi.nlm.nih.gov/23041195/); PubMed Central PMCID: PMC3494819.
106. Smith AM, Lewis BK, Ruttimann UE, Ye FQ, Sinnwell TM, Yang Y, et al. Investigation of low frequency drift in fMRI signal. *Neuroimage*. 1999; 9(5):526–33. <https://doi.org/10.1006/nimg.1999.0435> PMID: [10329292](https://pubmed.ncbi.nlm.nih.gov/10329292/).
107. Kay KN, Rokem A, Winawer J, Dougherty RF, Wandell BA. GLMdenoise: a fast, automated technique for denoising task-based fMRI data. *Frontiers in neuroscience*. 2013; 7:247. <https://doi.org/10.3389/fnins.2013.00247> PMID: [24381539](https://pubmed.ncbi.nlm.nih.gov/24381539/); PubMed Central PMCID: PMC3865440.
108. Dumoulin SO, Wandell BA. Population receptive field estimates in human visual cortex. *Neuroimage*. 2008; 39(2):647–60. <https://doi.org/10.1016/j.neuroimage.2007.09.034> PMID: [17977024](https://pubmed.ncbi.nlm.nih.gov/17977024/); PubMed Central PMCID: PMC3073038.
109. Winawer J, Horiguchi H, Sayres RA, Amano K, Wandell BA. Mapping hV4 and ventral occipital cortex: the venous eclipse. *Journal of vision*. 2010; 10(5):1. Epub 2010/07/10. <https://doi.org/10.1167/10.5.1> PMID: [20616143](https://pubmed.ncbi.nlm.nih.gov/20616143/); PubMed Central PMCID: PMC3033222.